catalysts

MDPI

Article

Synergistic Photothermal Catalysis over an MOF-Derived Matrix Enabled by Alloy-Coordination Interactions for Sustainable Hydrogen Production from Formic Acid

Shenghao Li [1], Siyu Song [1], Chunlin Ke [1], Zhengting Gu [1], Mingzheng Liao [2] and Chao Wang [1,*]

[1] Guangdong Provincial Key Laboratory on Functional Soft Condensed Matter, School of Materials and Energy, Guangdong University of Technology, Guangzhou 510006, China
[2] School of Ocean Engineering, Guangzhou Maritime University, Guangzhou 510700, China
* Correspondence: chaowang@gdut.edu.cn

Abstract

Formic acid (FA) has emerged as a promising liquid hydrogen storage material, yet efficient photothermal dehydrogenation catalysts with high activity and H_2 selectivity remain challenging. Herein, a polymetallic synergistic PdCu/M-ZNC (where M represents the co-doped In, Sn and Mo species) is fabricated by molten-salt-assisted pyrolysis of ZIF-8 precursors followed by metal incorporation. The unique molten salt environment effectively preserves the porous architecture of ZIF-8, enabling the secure anchoring of PdCu alloy nanoparticles onto the carbonaceous matrix enriched with M-N_x coordination sites. Under light irradiation, the PdCu alloy sites kinetically accelerated the overall adsorption and activation of FA molecules. Based on empirical observations and corroborated by the established literature, this alloying effect was inferred to facilitate the C-H bond cleavage and HCOO* desorption processes. Concurrently, the M-N_x sites act as efficient electron transfer channels, facilitating the rapid coupling of photogenerated electrons with protons (H^+) to evolve H_2. Consequently, the optimal catalyst exhibits an enhancement in gaseous product yield (404.46 mmol/g/h) and H_2 selectivity (67.49%) at 75 °C. This work offers a catalyst design that aligns with several principles of green chemistry: it maximizes the atom utilization of precious Pd, incorporates synergistic non-precious metals within MOF-derived frameworks to enhance stability, and leverages solar energy to drive hydrogen production under mild conditions, presenting a more sustainable pathway for hydrogen release from liquid carriers.

Keywords: metal–organic framework; photothermal hydrogen production; formic acid dehydrogenation

Academic Editor: Vladimir Sobolev

Received: 25 March 2026
Revised: 10 April 2026
Accepted: 17 April 2026
Published: 27 April 2026

1. Introduction

Hydrogen is an ideal energy carrier owing to its ultrahigh mass energy density [1] and holds great potential for replacing non-renewable energy sources. However, its low volumetric density renders storage and transportation major bottlenecks for practical applications [2]. Currently, researchers have explored various pathways for hydrogen production. While water electrolysis [3–5] and photocatalytic water splitting [6–9] represent paradigmatic strategies for green hydrogen production, their large-scale implementation is frequently hampered by thermodynamically intensive energy consumption and sluggish solar-to-chemical conversion efficiencies, respectively. Meanwhile, although ammonia decomposition offers a promising hydrogen storage solution [10,11], the inherent toxic and

corrosive nature of ammonia imposes stringent infrastructural and safety management requirements. In stark contrast to these approaches, formic acid dehydrogenation stands out as a highly compelling alternative. Formic acid (FA) has emerged as a high-performance liquid hydrogen carrier that attracts considerable attention due to its non-toxicity, high hydrogen storage capacity and excellent stability [12]. Hydrogen stored in formic acid can be released via dehydrogenation reaction with a low enthalpy change (30 kJ mol^{-1}) that enables thermodynamically favorable hydrogen production at low temperatures [13]. Traditional thermally driven liquid–solid dehydrogenation via thermal catalysis, however, suffers from high energy consumption and inadequate stability [14]. As a sustainable alternative, photothermal catalytic hydrogen production is recognized as one of the most promising strategies [15]. Notably photothermal catalysis differs significantly from both photocatalysis and thermal catalysis. Thermal catalysis relies solely on thermal energy to drive reactions [16], while photocatalysis depends on photogenerated electron–hole pairs for reaction initiation [17], and photothermal catalysis combines photothermal conversion with photo-thermal synergistic effects to accelerate the reaction [18]. The development of photothermal catalysts for formic acid dehydrogenation still encounters certain limitations. Existing systems frequently favor single-metal or single-component active sites, which may restrict the electronic synergy and functional complementarity among multiple metals, thereby making it challenging to simultaneously optimize several key performance metrics [19]. In addition, support structure designs generally focus on the dispersion of single metals, often falling short of providing an integrated architecture capable of delivering polymetallic anchoring sites and efficient electron transfer channels [20]. Thus, developing photothermal catalysts with stable active sites and efficient synergistic regulation mechanisms is critical for advancing the practical application of formic-acid-based hydrogen production technology.

To date, the rational design of heterogeneous catalysts for formic acid dehydrogenation has encompassed a wide spectrum of metals. While recent endeavors have established that catalytic architectures based on other active metals, specifically including Cu [21], Ce [22] and Au [23,24], can also deliver remarkable catalytic efficacy and high H_2 selectivity, Pd-based systems persistently stand out as the pre-eminent choice for formic acid dehydrogenation. Pd-based catalysts stand out as the most efficient heterogeneous catalysts for formic acid dehydrogenation, with Pd/C widely utilized due to its simple composition and industrial scalability [25]. However, their high precious metal content leads to substantial costs. Formic acid dehydrogenation entails three interconnected key steps: C-H bond activation, H* recombination and CO poisoning suppression. Single-metal catalysts struggle to simultaneously optimize these competing processes. Thus, introducing non-precious metals to construct a palladium-based multi-metal system is imperative for achieving synergistic division of reaction pathways. Specifically, Pd primarily mediates C-H bond activation, Cu promotes H* recombination via modulating the electronic structure of Pd [26], and metals such as In, Sn and Mo suppress CO adsorption on active sites [27–29]. Notably the efficient synergy among these multi-metal components relies heavily on high-performance catalyst supports. Catalyst support plays a pivotal role in heterogeneous catalysis, and metal–support interactions exert a profound influence on catalytic performance [30].

Metal–organic frameworks (MOFs), a new class of porous coordination polymers, stand out as superior support for photothermal catalysis. Unlike traditional carbon supports with limited photothermal conversion efficiency and oxide supports that are prone to metal aggregation, MOFs possess intrinsic advantages including structural tunability ultrahigh specific surface area and multifunctional surface groups [31]. Importantly, MOFs generally preserve their intrinsic porous structural features during controlled pyrolysis [32]. This

process yields highly porous support materials, such as nitrogen-doped carbon, which are characterized by extensive specific surface areas, hierarchical pore networks, and uniformly distributed active centers. This uniquely derived architecture provides a stable foundation to anchor polymetallic components, thereby promoting uniform dispersion and significantly mitigating nanoparticle agglomeration [33]. Furthermore, these tailored pore structures can optimize mass transfer dynamics, facilitating the efficient diffusion of reactants toward the catalytic active sites [34]. Against this backdrop, the development of easily prepared catalysts capable of multi-metal loading has become a pressing imperative.

Based on these considerations, this study employed ZIF-8 as a precursor to prepare a ZIF-derived nitrogen-doped carbon (ZNC) support via molten-salt-assisted pyrolysis. Pd, Cu, In, Sn, and Mo were introduced onto the ZNC support to construct a PdCu/M-ZNC (where M represents the co-doped In, Sn and Mo species) polymetallic synergistic catalyst. The PdCu alloy acts as the core catalytic active site governing the formic acid dehydrogenation reaction. In, Sn and Mo form stable M-N_x coordination structures with pyridinic nitrogen in the support which serve as efficient electron transport channels. This architecture aims to reduce reliance on precious Pd through electronic synergy with Cu while utilizing the ZNC framework derived from a templated MOF to minimize waste in catalyst preparation, as well as harnessing photothermal energy to achieve efficient dehydrogenation at a significantly lower bulk temperature than conventional thermal catalysis, thereby lowering the overall energy footprint of the hydrogen release process. Meanwhile, the synergistic catalytic mechanism regulated by metal–support interactions between the metals and the MOF-derived support was investigated, providing new insights for the development of advanced photothermal catalysts.

2. Results and Discussion

SEM images (Figure 1a) revealed that ZIF-8 exhibited a typical dodecahedral morphology, consistent with the sodalite (SOD) topological structure [35]. The Pd-MO_x/ZIF-8 sample prepared by introducing a metal precursor completely collapsed from its originally clear dodecahedral structure. This severe morphological destruction was attributed to the acidic environment during the metal loading process. When the pristine ZIF-8 was exposed to the acidic precursor solution, it triggered severe hydrolysis and etching of the Zn-N coordination bonds, thereby destroying its intrinsic thermodynamic and structural stability [36,37]. Ultimately, this led to structural collapse and carbonization of ZIF-8 in a reducing atmosphere at 400 °C. After pyrolysis, the ZIF-8 surface became rougher yet largely retained its original morphology, and the resulting product was denoted as ZNC. Strikingly, the SEM image of the PdCu/M-ZNC sample demonstrates that its morphological structure is successfully preserved, highlighting the excellent structural robustness of the pyrolyzed carbon matrix.

X-ray diffraction (XRD) measurements were performed to characterize the phase compositions of the synthesized samples. As shown in Figure 1b, the XRD pattern of ZIF-8 matched well with the literature reports [38]. The other three samples display a high degree of carbonization, with a diffraction peak at 20.86° assigned to the (002) crystal plane of graphitic carbon, a characteristic peak corresponding to graphitic carbon interlayer stacking [39]. Additionally, the PdCu/M-ZNC sample exhibited distinct diffraction peaks at 41.42° and 48.21° corresponding to the (111) and (200) crystal planes of the face-centered cubic PdCu alloy. To demonstrate the successful formation of the PdCu alloy, the XRD pattern of the Pd/M-ZNC reference sample was also evaluated for comparison (Figure S1). The (111) and (200) characteristic diffraction peaks of pure Pd in the Pd/M-ZNC sample are located at approximately 40.11° and 46.66°. In contrast, the corresponding peaks for the PdCu/M-ZNC catalyst were noticeably shifted to higher 2θ angles. This distinct positive

shift served as a classic crystallographic signature of alloy formation. The Scherrer equation ($D = K\lambda/\beta\cos\theta$) was used to analyze two diffraction peaks in the PdCu/M-ZNC sample. For the primary PdCu (111) peak at $2\theta = 41.42°$, peak fitting yielded a full width at half maximum (FWHM, β) of 1.379°. The calculated crystallite size $D_{(111)}$ is 6.09 nm. For the secondary PdCu (200) peak at $2\theta = 48.21°$, the FWHM was fitted as 0.794°, yielding a crystallite size $D_{(200)}$ of 10.84 nm. The average crystallite size derived from XRD is roughly 8.47 nm. The formation of the PdCu alloy phase promoted electron transfer from Cu to Pd, weakened the excessive adsorption of HCOOH intermediates on Pd, and thereby accelerated the catalytic reaction [40]. In addition, to identify the metal oxide species of Pd-MO_x/ZIF-8, its high-resolution XRD pattern was shown in Figure S2. No distinct diffraction peaks corresponding to metal oxide phases were observed in the XRD pattern of the Pd-MO_x/ZIF-8. The absence of these diffraction signals indicated that the metal oxides in the Pd-MO_x/ZIF-8 system were likely formed as extremely small, highly dispersed nanoclusters on the support, with domain sizes falling well below the XRD detection threshold [41,42]. The complementary XPS results provided direct and conclusive evidence for the successful formation of highly dispersed MO_x species on the support, with the corresponding XPS spectra to be discussed in detail later.

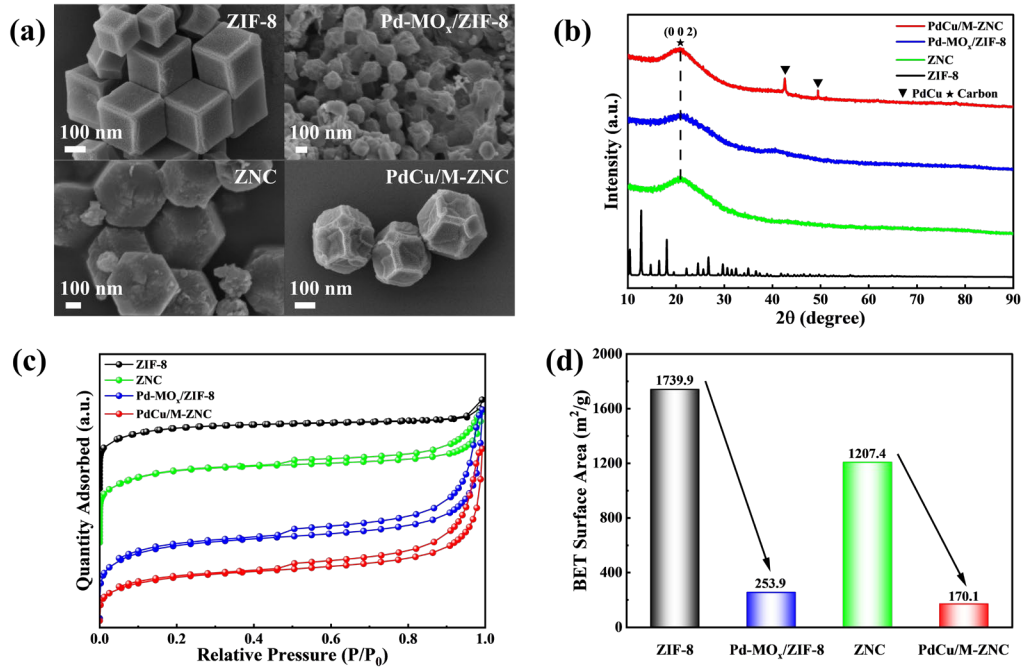

Figure 1. (**a**) SEM image, (**b**) XRD pattern, (**c**) N_2 adsorption–desorption isotherm and (**d**) BET specific surface area data of the samples.

Brunauer–Emmett–Teller (BET) measurements were performed to investigate the pore size distribution (Figure 1c) and specific surface area (Figure 1d) of the catalysts. The ZIF-8 sample exhibited a high specific surface area of 1739.9 m^2/g. Its N_2 adsorption isotherm reached a plateau at low relative pressure and remained stable in the subsequent high-pressure region, indicating that the ZIF-8 structure is almost entirely composed of micropores [43]. After pyrolysis, the resulting ZNC sample displayed a type IV N_2 adsorption–desorption isotherm [44] with a distinct hysteresis loop in the relative pressure range of 0.4–0.9, accompanied by a specific surface area of 1207.35 m^2/g. Notably, ZNC inherited the ultrahigh specific surface area of ZIF-8 while acquiring a mesoporous structure. Furthermore, the specific surface areas of PdCu-MO_x/ZIF-8 and PdCu/M-ZNC were determined to be 253.9 m^2/g and 170.1 m^2/g, respectively. This result indicated that the ZIF-derived nitrogen-doped carbon support offers advantages in effective metal loading

and mass transfer accessibility. Although ZNC, PdCu/M-ZNC and Pd-MO_x/ZIF-8 all contain mesopores, the introduction of mesoporosity in these three samples is attributed to two distinct structural evolution pathways depending on their specific treatments. The mesoporosity in these samples originates from the molten-salt-assisted pyrolysis process. During pyrolysis at 730 °C, the KCl-KBr molten salt acts as a liquid template that effectively suppresses carbon framework shrinkage and preserves high porosity. Concurrently, the ZIF-8 framework undergoes pyrolysis. The Zn(II) species are converted into zinc salts ($ZnCl_2$) and are subsequently removed during the washing step. The dissolution of these zinc salts, combined with the molten salt templating effect, leaves behind abundant structural voids. This process transforms the intrinsic micropores into a mesoporous structure. Consequently, ZNC displays a type IV N_2 adsorption–desorption isotherm with a distinct hysteresis loop and inherits the ultrahigh specific surface area of ZIF-8 while acquiring a mesoporous structure. The PdCu/M-ZNC catalyst inherits this architecture. The elemental compositions of PdCu/M-ZNC were determined using inductively coupled plasma optical emission spectroscopy (ICP-OES). For the PdCu/M-ZNC sample, the ICP-OES analysis (Tables S1 and S2) confirms that the total metal loading was determined to be approximately 9 wt.%, closely aligning with the theoretical nominal loading of 10 wt.%. Furthermore, the actual molar ratio of Pd:Cu:In:Sn:Mo is approximately 0.182:0.178:0.184:0.180:0.177, which matches our intended design ratio of 1:1:1:1:1. This precise compositional match is fundamentally attributed to the exceptional chemical and thermal stability of the molten-salt-derived ZNC carbon support. In contrast, the source of mesopores in the Pd-MO_x/ZIF-8 sample is quite different. During the metal loading process, the pure ZIF-8 support was stirred in a 0.1 M HCl solution containing $PdCl_2$ and $SnCl_4$. This acidic environment caused etching and hydrolysis of the coordination bonds [45]. The acidic etching process creates structural defects and forms mesopores within the original microporous matrix. This may compromise its intrinsic thermodynamic stability, rendering the framework highly susceptible to structural collapse and carbonization at merely 400 °C.

Figure 2a showed the Raman spectra of ZIF-8, which were dominated by intense bands corresponding to methyl group and imidazole ring vibrations. The band observed at 689 cm^{-1} was assigned to imidazolium ring puckering stretching, while the bands observed at 1028, 1150, 1463, and 1509 cm^{-1} were attributed to imidazolium ring puckering, C-N stretching, and -CH_3 and C-C bending, respectively [46,47]. The other three samples all displayed D peaks associated with defect sites in carbon materials and G peaks related to the graphitization degree of carbon materials at 1333 cm^{-1} and 1579 cm^{-1}. Among these samples, ZNC exhibited the highest I_D/I_G ratio (1.06), likely due to Zn loss at elevated temperatures that exposes abundant defect sites. Notably, PdCu/M-ZNC showed the lowest I_D/I_G ratio (0.96), indicating a higher graphitization degree and fewer structural defects. This phenomenon could be attributed to the graphitization-promoting effect of metals in the ZNC support, which induced the formation of a more ordered carbon layer [48]. Beyond providing a high specific surface area, the hierarchical pore structure and defect-rich carbon framework are expected to influence catalytic behavior through improved reactant accessibility and enhanced interfacial contact between metal species and the carbon support. Such structural features have been reported to facilitate rapid mass transport of liquid-phase reactants and gaseous products [49,50], which is particularly relevant for formic acid dehydrogenation, where intermediate accumulation and product desorption can become kinetically limiting under mild conditions.

Fourier transform infrared (FTIR) spectroscopy (Figure 2b) was used to characterize the functional group information of the samples. A strong and broad absorption band at 3400 cm^{-1} was observed in all samples, corresponding to O-H stretching vibrations from adsorbed water or moisture, possibly induced by exposure to the atmosphere [51].

The ZIF-8 sample exhibited bending vibration signals of C=C and C=N at 1305 cm^{-1} and 1424 cm^{-1}, respectively, with peaks in the 750–1200 cm^{-1} range primarily assigned to stretching vibrations of the entire imidazole ring. Additionally, the absorption band near 687 cm^{-1} was attributed to Zn-centered Zn-N stretching vibrations in ZIF-8 [52,53]. An intense peak at 1600 cm^{-1} was attributed to C-C bonds in the carbon substrate, and the persistence of this high-intensity peak at elevated temperatures indicates thermally stable carbon frameworks [54]. Notably, the signals of C-C and C=N bonds in the Pd-MO_x/ZIF-8 sample were significantly lower, attributed to the etching and hydrolysis of the ZIF-8 framework in the acidic metal precursor solution, followed by collapse and partial carbonization at low reduction temperatures. In contrast, the carbon–nitrogen framework of pyrolyzed ZNC series samples underwent reconstruction at high temperatures. C-N and C-C stretching vibration signals near 1240 cm^{-1} and 1593 cm^{-1} were assigned to pyridine nitrogen active sites and graphitic carbon in the nitrogen-doped carbon support, respectively. The significant attenuation of the Zn-N signal indicated that complete pyrolysis occurred in ZIF-8. The Zn species existed as $ZnCl_2$ and were removed during washing.

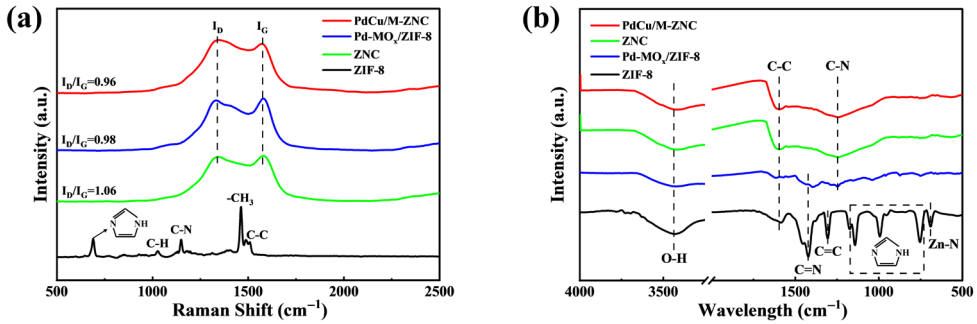

Figure 2. (**a**) Raman spectra and (**b**) Fourier transform infrared spectroscopy of the samples.

Energy-dispersive X-ray spectroscopy (EDS) mappings (Figure 3a,d) reveal overlapping signals of Pd, Cu, In, Sn, and Mo across the same regions in both samples, confirming the successful loading of all five metal components. Transmission electron microscopy (TEM) images (Figure 3b) showed that PdCu/M-ZNC comprises regular high-density metal nanoparticle aggregates uniformly dispersed on the carbon–nitrogen matrix without significant agglomeration and with an average particle size of 6.65 nm (Figure 3c). This result was in good agreement with the crystallite size estimated by XRD in Figure 1b. This uniform dispersion was attributed to the hierarchical porous structure (micropores and mesopores) of ZNC, which provides abundant anchoring sites and enhances the dispersibility of metal species. Transmission electron microscopy (TEM) images (Figure 3e) of the Pd-MO_x/ZIF-8 sample present metal particles loaded on ZIF-8 with an average size of 2.86 nm (Figure 3f).

X-ray photoelectron spectroscopy (XPS) was employed to analyze the electronic structures and valence states of PdCu/M-ZNC and Pd-MO_x/ZIF-8. The C 1s XPS spectrum (Figure 4a) revealed peaks at 284.6 eV, 286.3 eV and 288.3 eV, corresponding to C-C, C-N and C-O bonds, respectively. These results suggested the presence of carbon-based species in the carbonized product. Figure 4b shows the N 1s spectrum, where the peaks at 398.6 eV and 400.7 eV correspond to pyridine nitrogen and pyrrole nitrogen, respectively, with their lone pair electrons serving as anchoring points for the metals [55]. Furthermore, the peak at 402.7 eV in PdCu/M-ZNC corresponds to graphitic nitrogen, indicating a high degree of graphitization of the ZNC support after surface pyrolysis, which is consistent with the Raman spectroscopy characterization results (Figure 2a). High-resolution Pd 3d XPS spectra (Figure 4c) were deconvoluted into two doublets. For the Pd-MO_x/ZIF-8 sample, these doublets were identified at 335.2/340.4 eV and 337.3/342.2 eV, corresponding to

metallic Pd^0 and Pd^{2+} species, respectively [56]. In contrast, the PdCu/M-ZNC samples exhibited a significant downshift in the binding energy of Pd^0 peaks due to PdCu alloy formation, with the Pd^0 doublet located at 334.7 eV and 336.4 eV. These results confirm effective electron transfer from Cu to Pd which arises from PdCu alloy formation and the lower electronegativity of Cu compared to Pd [57–59]. This electronic state is known to weaken the strong adsorption of CO-like intermediates, a key step in suppressing the dehydration side reaction and enhancing H_2 selectivity [60]. High-resolution Cu 2p XPS spectra (Figure 4d) were also deconvoluted into two doublets. For the PdCu/M-ZNC sample, these doublets appeared at 932.6/952.4 eV and 935.5/955.4 eV, assigned to metallic Cu and Cu^{2+} species, respectively [61]. In contrast, the Pd-MO_x/ZIF-8 sample showed only two peaks at 935.6 eV and 954.9 eV, indicating that Cu existed solely as oxides without forming an alloy with Pd. The reason for this arrested reduction in the Pd-MO_x/ZIF-8 system lies in the specific coordination environment and the resulting kinetic barriers. During the pre-reduction phase, the copper species form robust Cu–O bonds with the structural defects of the MO_x/ZIF-8 framework. This strong interfacial coordination induces a pronounced strong metal–support interaction (SMSI). As reported in the literature, such SMSI effects significantly shift the reduction peaks of these stabilized copper species to higher temperatures [62]. Therefore, despite the presence of Pd, the copper species remain thermodynamically trapped in their oxidized state within the pristine ZIF-8 architecture.

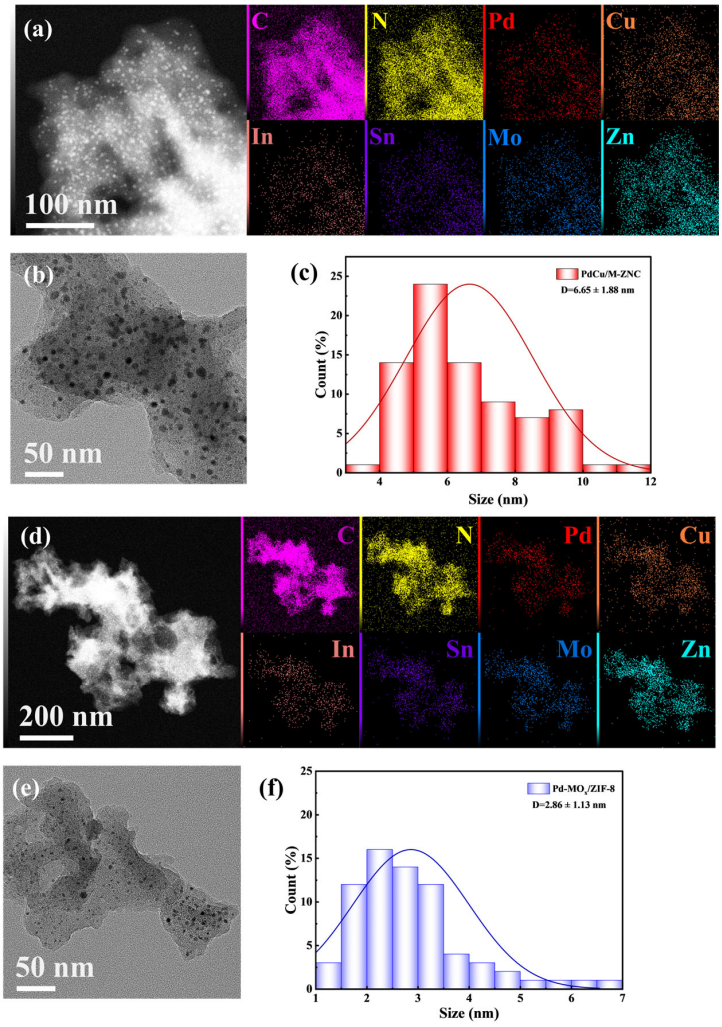

Figure 3. (**a**) EDS elemental mapping images, (**b**) TEM image and (**c**) particle size distribution diagram of PdCu/M-ZNC. (**d**) EDS elemental mapping images, (**e**) TEM image and (**f**) particle size distribution diagram of Pd-MO_x/ZIF-8.

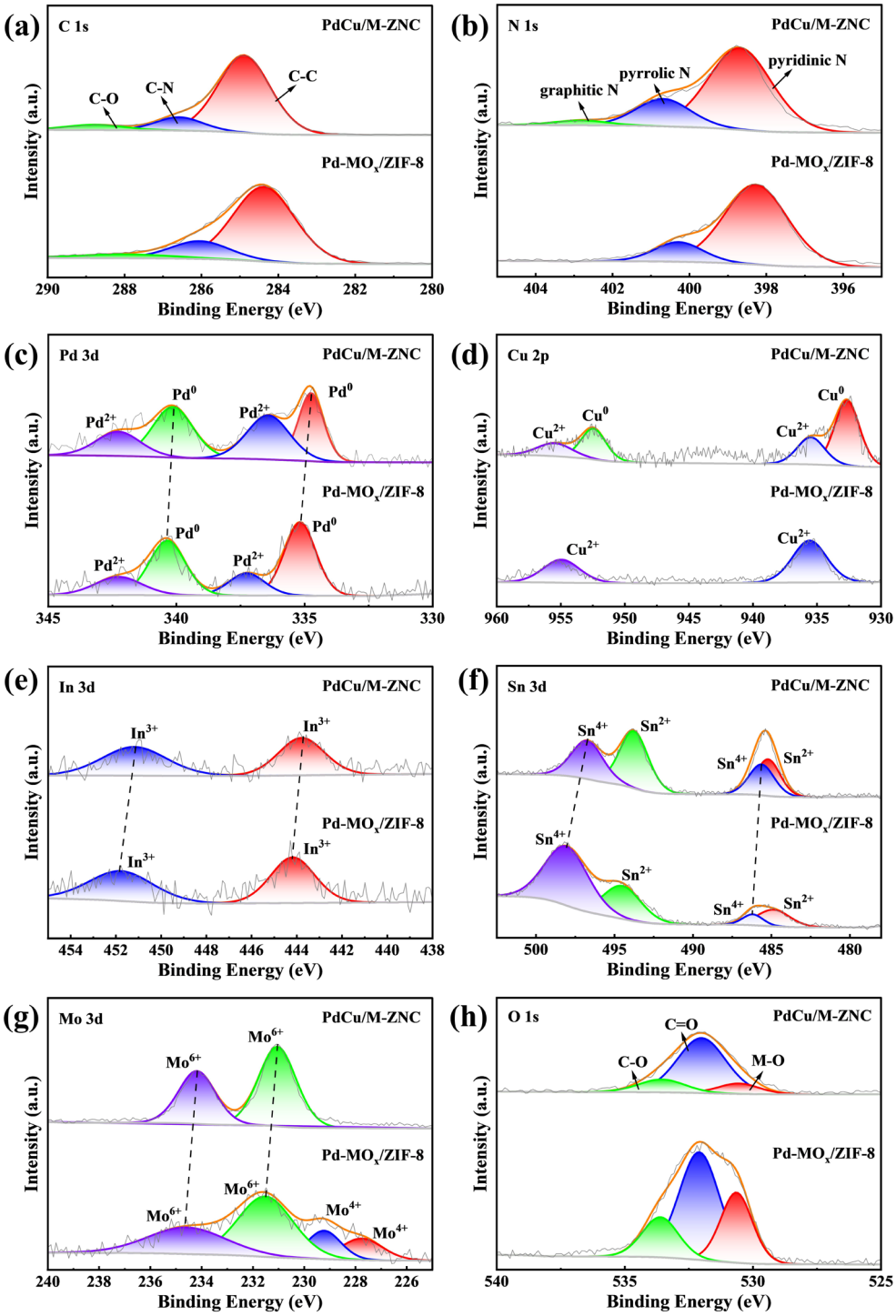

Figure 4. High-resolution XPS profiles of the (**a**) C 1s, (**b**) N 1s, (**c**) Pd 3d, (**d**) Cu 2p, (**e**) In 3d, (**f**) Sn 3d, (**g**) Mo 3d, and (**h**) O 1s electrons of PdCu/M-ZNC and Pd-MO_x/ZIF-8.

High-resolution In 3d XPS spectra (Figure 4e) revealed two characteristic peaks for both samples. For the Pd-MO_x/ZIF-8 sample, these peaks were located at 444.2 eV and 451.8 eV, corresponding to indium oxide species. In contrast, the PdCu/M-ZNC sample exhibited these peaks at 443.7 eV and 450.8 eV, with a distinct downshift in binding energy, which is indicative of the In-N coordination configuration [63]. In the In-N coordination environment, the less electronegative nitrogen atoms withdraw less electron density from the central indium atom. Consequently, compared to the indium atoms in indium oxide, the indium atoms in the In-N coordination retain a higher surrounding electron density.

This enriched local electron density enhances the nuclear shielding effect, which induces a negative chemical shift, moving the binding energy toward a lower energy direction [64,65]. No obvious In^0 peak was detected in either sample. This observation was attributed to the strong coordination interaction between In^{3+} and the lone pair electrons of nitrogen atoms in the carbon–nitrogen support, which inhibits In^{3+} from accepting electrons from H_2 and escaping the coordination environment to be reduced to In^0. Peak fitting of the Sn 3d XPS spectra (Figure 4f) revealed two doublets, confirming that Sn species in both PdCu/M-ZNC and Pd-MO_x/ZIF-8 samples existed as Sn^{4+} and Sn^{2+}. Notably, the Sn^{4+} peaks in PdCu/M-ZNC exhibited a downshift in binding energy relative to those in Pd-MO_x/ZIF-8, confirming the formation of Sn-N bonds [66]. Both samples also displayed Sn^{2+} peaks. This phenomenon can perhaps be attributed to the partial reduction of Sn^{4+} to Sn^{2+} by hydrogen during sample preparation. These facts provide strong evidence for their coordination to nitrogen in the ZNC matrix (forming M-N_x). Mo 3d XPS spectra (Figure 4g) exhibited characteristic peaks corresponding to Mo^{6+} species. Comparative analysis revealed that the Mo^{6+} peaks in PdCu/M-ZNC samples also displayed a downshift in binding energy. As a high-valence cation, Mo^{6+} interacts strongly with nitrogen atoms in the support, forming a Mo-N coordination structure which enhances the electron cloud density around Mo^{6+} [67].

The high-resolution O 1s XPS spectra were systematically analyzed (Figure 4h). For the Pd-MO_x/ZIF-8 sample, the O 1s spectrum exhibits a prominent peak at a lower binding energy of approximately 530.6 eV, which is the classic signature of lattice oxygen. The strong intensity of this peak unambiguously confirms the extensive formation of metal–oxygen (M-O) bonds on the partially pyrolyzed ZIF-8 support. In stark contrast, the O 1s spectrum of the final PdCu/M-ZNC catalyst displays a dramatic attenuation in the intensity of this M-O lattice oxygen peak. Instead, the spectrum is dominated by peaks at high binding energies, typically attributed to C=O and C-O oxygen-containing functional groups on the carbon matrix. As mentioned above, the intensity of the oxygen peak in the M-O lattice of the PdCu/M-ZNC catalyst is significantly reduced in the O 1s spectrum. Simultaneously, compared to Pd-MO_x/ZIF-8, the binding energies of In, Sn, and Mo species all shift significantly to lower energies. From an electronic perspective, nitrogen is relatively less electronegative than oxygen. Therefore, when these metal cations coordinate with nitrogen atoms rather than oxygen atoms, they gain more electrons from the nitrogen ligands. The increased electron cloud density around the metal atoms essentially manifests as a negative shift in the observed binding energy. Therefore, the significant weakening of the M-O bond and the reduction in the binding energies of In, Sn, and Mo species indicate that the vast majority of metal species have been successfully anchored in the nitrogen-doped carbon network, forming a stable M-N coordination structure. Such atomic-scale integration of heterometals into a conductive carbon framework creates efficient electron transfer pathways [68]. During photothermal catalysis, these pathways likely serve as highways for photogenerated electrons from the carbon support to rapidly reach the PdCu active sites or adsorbed H* intermediates. This process, akin to a built-in electron transfer chain, can significantly accelerate the rate-determining H* recombination step for H_2 evolution [69], while the localized heat from photothermal conversion lowers the barrier for the initial C-H bond activation. Crucially, the distinct binding energy downshifts observed in the In 3d, Sn 3d and Mo 3d spectra (Figure 4e–g) imply more than just the formation of M-N bonds; they indicate a robust electronic metal–support interaction (EMSI) [70]. In the context of heterogeneous catalysis, these N-coordinated high-valence metal species (In^{3+}, Sn^{4+} and Mo^{6+}) function as 'electronic anchors.' By modulating the local electron density, these sites create strong interfacial bonding that traps PdCu nanoparticles, effectively suppressing Ostwald ripening and metal leaching during the thermal reduction process [71]. This electronic anchoring mechanism provides a plausible explanation for the

excellent dispersion of PdCu nanoparticles (6.65 nm) observed in TEM (Figure 3b), despite the high-temperature treatment. Such a 'geometric–electronic' dual-stabilization strategy is fundamental to ensuring long-term catalyst durability, addressing a critical challenge in the design of sustainable catalytic systems.

In order to investigate the charge separation capability, a key indicator of the catalyst's optoelectronic conversion performance, photocurrent measurements were performed under intermittent illumination (Figure 5a). The results revealed that PdCu/M-ZNC exhibited significantly higher photocurrent intensity and faster response kinetics than Pd-MO_x/ZIF-8, indicating enhanced charge separation efficiency and photogenerated electron transfer dynamics. This enhancement was attributed to the strong metal–support interaction formed between the metal species and nitrogen-doped sites in the carbon–nitrogen framework [72]. Specifically, the lone pair electrons of nitrogen atoms form M-N coordination bonds with In, Sn, and Mo. This interaction established efficient metal–support electron transport channels, facilitating the transfer of photogenerated electrons on the catalyst surface and suppressing photogenerated carrier recombination, which ultimately contributed to the higher photocurrent intensity [73]. In the formic acid photothermal hydrogen production system, efficient charge separation ensured adequate availability of photogenerated electrons as active species for driving the formic acid dehydrogenation reaction. The H* intermediates generated during the reaction accept photogenerated electrons for rapid desorption, thereby promoting H_2 evolution [74]. The photoluminescence signal (Figure 5b) primarily corresponds to the radiative recombination of photogenerated electron–hole pairs within the nitrogen-doped carbon matrix. During the pyrolysis and carbonization process of ZIF-8, the organic 2-methylimidazole linkers are transformed into a carbon–nitrogen framework. This framework possesses abundant structural defects and nitrogen-containing species, which act as the luminescent centers upon optical excitation. Steady-state photoluminescence (PL) spectroscopy results showed a significant decrease in PL peak intensity for the PdCu/M-ZNC sample, indicating a marked reduction in the recombination probability of photogenerated electron–hole pairs. This phenomenon reflected the strong interaction between metal components and the nitrogen-doped carbon framework, which effectively inhibited the non-radiative recombination of photogenerated carriers and thus significantly improved the utilization efficiency of photogenerated charge carriers. These results were consistent with the I-t photocurrent response data (Figure 5a), further verifying that the strong interaction between multi-metal components and the nitrogen-doped carbon framework optimizes the charge separation behavior and thereby enhances the photothermal catalytic performance. To elucidate the interfacial charge transfer kinetics and validate the proposed electron transfer pathways, electrochemical impedance spectroscopy (EIS) measurements were conducted. As presented in Figure S3, the semicircular arc radius of the PdCu/M-ZNC catalyst was significantly smaller than that of the Pd-MO_x/ZIF-8. The calculated charge transfer resistance for PdCu/M-ZNC was remarkably low at 43 Ω, which is substantially reduced compared to the 181 Ω observed for Pd-MO_x/ZIF-8. This dramatically diminished impedance provides compelling direct evidence that the polymetallic M-N_x coordination sites within the nitrogen-doped carbon framework effectively construct highly efficient electron transfer channels, thereby facilitating rapid interfacial charge transfer dynamics. While enhanced photocurrent response and suppressed photoluminescence intensity are indicative of improved charge separation efficiency, it should be noted that these measurements alone do not directly confirm the participation of photoexcited electrons in specific elementary reaction steps. However, when interpreted together with catalytic performance trends, these optoelectronic features suggest a higher probability of charge utilization at the catalyst surface. In photothermal catalytic systems, such improved charge availability has been widely associated with facilitated electron transfer to

surface intermediates, particularly in reactions involving proton-coupled electron transfer processes [75], such as formic acid dehydrogenation.

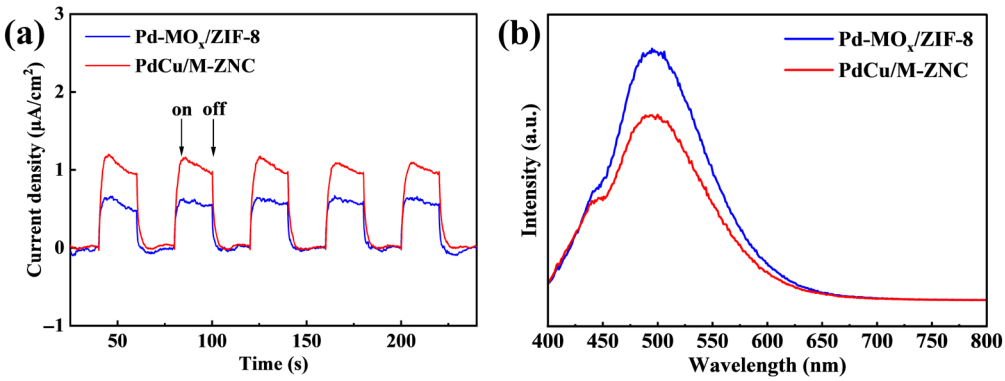

Figure 5. (**a**) Transient photocurrent densities and (**b**) steady-state PL spectra of Pd-MO$_x$/ZIF-8 and PdCu/M-ZNC.

The UV–vis absorption spectra (Figure 6a) revealed that Pd-MO$_x$/ZIF-8 exhibits relatively limited optical absorption, with its predominant absorption band located in the ultraviolet region (<400 nm). This limited optical response is likely dictated by the intrinsic wide bandgap of the MOF. In addition, the PdCu/M-ZNC catalyst displays a dramatically enhanced and broadened absorption profile spanning the entire UV and visible light regions. This remarkable panchromatic broadband absorption is mainly attributed to the transformation of the MOF into a highly graphitized nitrogen-doped carbon matrix, which, in conjunction with the strong light absorption capabilities of the PdCu alloy nanoparticles, contributes to this transformation. To quantitatively evaluate this evolution, a Tauc plot (Figure 6b) was constructed based on the Kubelka–Munk function. The optical bandgap of the optimized PdCu/M-ZNC catalyst is significantly narrowed to 1.44 eV, compared to the relatively large bandgap of 2.26 eV for the Pd-MO$_x$/ZIF-8. This drastically narrowed bandgap intrinsically facilitates efficient photoexcitation under lower-energy photon irradiation.

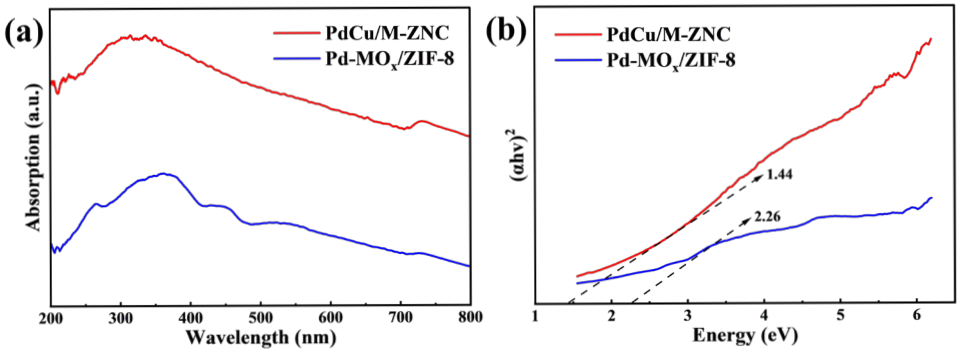

Figure 6. (**a**) UV−vis diffuse reflectance spectra and (**b**) Tauc plot of Pd-MO$_x$/ZIF-8 and PdCu/M-ZNC.

To evaluate the photothermal catalytic performance of Pd-MO$_x$/ZIF-8 and PdCu/M-ZNC catalysts, formic acid dehydrogenation to hydrogen experiments were performed using a xenon lamp as the light source. This work focused on the effects of temperature gradient variations and light on/off conditions on key reaction metrics including gaseous product yield (Figure 7a), formic acid conversion (Figure 7b) and hydrogen selectivity (Figure 7c). Regardless of light irradiation, formic acid conversion, gaseous product yield and hydrogen selectivity of both catalysts increased continuously in the temperature range of 60 °C to 75 °C. This trend stems from the endothermic character of formic acid dehy-

drogenation, where elevated temperatures accelerate the reaction kinetics [76]. Under completely dark conditions, both catalysts showed low gaseous product yields and hydrogen selectivity. With light irradiation, these metrics improved, and PdCu/M-ZNC exhibited superior performance over Pd-MO_x/ZIF-8. Under the optimal experimental conditions of 75 °C with continuous illumination, the gaseous product yield over the PdCu/M-ZNC catalyst exhibited a substantial increase from 259.82 to 404.46 mmol/g/h. Concurrently, H_2 selectivity improved from 42.06% to 67.49%, achieving turnover frequency (TOF) of approximately 969.90 h^{-1} (Table S4). A comparable photo enhancement was also observed for the Pd-MO_x/ZIF-8 catalyst, where the gas production rate rose from 166.07 to 278.57 mmol/g/h, alongside an increase in H_2 selectivity from 23.19% to 47.68%. The absence of CO by-product was further rigorously confirmed by gas chromatograms (Figure S4), where the CO signal remained below the detection limit under all tested conditions. Furthermore, as shown in Figure S5, the apparent activation energy (E_a) was calculated based on the Arrhenius equation (Equation S3). The kinetic analysis revealed that the E_a of the PdCu/M-ZNC catalyst decreased from 38.26 kJ/mol under dark conditions to 35.06 kJ/mol under illumination. A similar trend was mirrored by the Pd-MO_x/ZIF-8 catalyst, which exhibited an E_a reduction from 49.20 to 43.96 kJ/mol upon light irradiation. Collectively, these experiments suggest that the photoinduced effect may effectively lower the apparent reaction barrier for the rate-determining step, which was highly likely associated with the C-H bond cleavage. In addition, the catalytic performance of PdCu/M-ZNC and Pd-MO_x/ZIF-8 was placed in the context of reported Pd-based catalysts for formic acid dehydrogenation. A quantitative comparison of H_2 + CO_2 evolution rate under representative reaction conditions is summarized in Figure S11 and Table S9. The low-Pd-loading polymetallic PdCu/M-ZNC and Pd-MO_x/ZIF-8 catalysts exhibited formic acid dehydrogenation performance comparable to previously reported Pd-based systems [77–80].

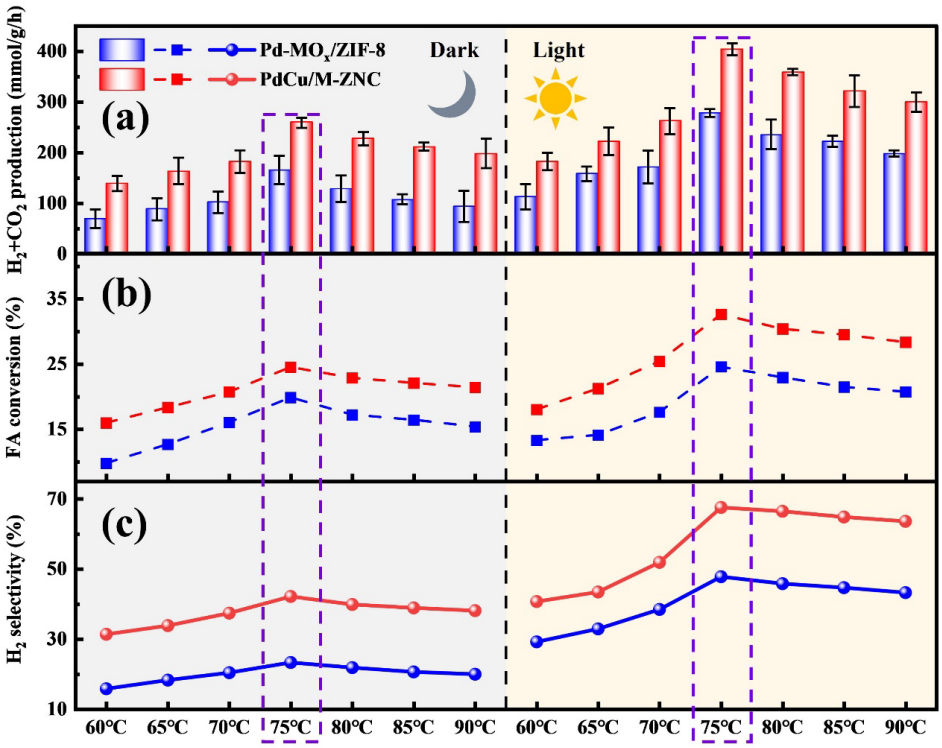

Figure 7. (**a**) H_2 + CO_2 production, (**b**) FA conversion and (**c**) H_2 selectivity of FA dehydrogenation over Pd-MO_x/ZIF-8 and PdCu/M-ZNC. Reaction conditions: catalyst mass: 0.1 g; reaction solution:

10 mL of an aqueous mixture containing formic acid–sodium formate mixture (n_{FA}:n_{SF} = 1:1, 2 mmol FA); reaction time: 5 min; irradiation: 300 W xenon lamp equipped with an AM 1.5G filter (100 mW cm^{-2}); temperature was controlled via a thermostatic oil bath. The evolved gas volume was quantified using the water displacement method, and the gas composition was analyzed by GC equipped with TCD and FID.

To unambiguously decouple the purely thermal and non-thermal effects and verify the concurrent presence of a photochemical pathway under light irradiation, specific charge-carrier trapping experiments were conducted using triethanolamine (TEOA) as a targeted hole scavenger [81]. As shown in Figure 8a, upon the addition of TEOA, the gas production rate over the PdCu/M-ZNC catalyst decreased from 404.46 to 321.43 mmol/g/h. A similarly severe suppression (from 278.57 to 176.79 mmol/g/h) was observed for the Pd-MO_x/ZIF-8 reference. If the light-induced enhancement were solely driven by localized thermoplasmonic heating, the addition of a trace amount of TEOA would not significantly alter the local temperature gradient, and thus the catalytic activity should remain largely unaffected. The decline in gas production demonstrates that a photochemical pathway is concurrently active. In a typical photocatalytic formic acid reaction, formic acid acts as a hole scavenger [82]. It is oxidized by photogenerated holes to release protons, which are then reduced to hydrogen gas by photogenerated electrons at the PdCu active sites. When TEOA is introduced, it fiercely competes with formic acid for the photogenerated holes. The consumption of holes by TEOA blocks this photochemical pathway of formic acid, consequently resulting in a decrease in the overall gas yield.

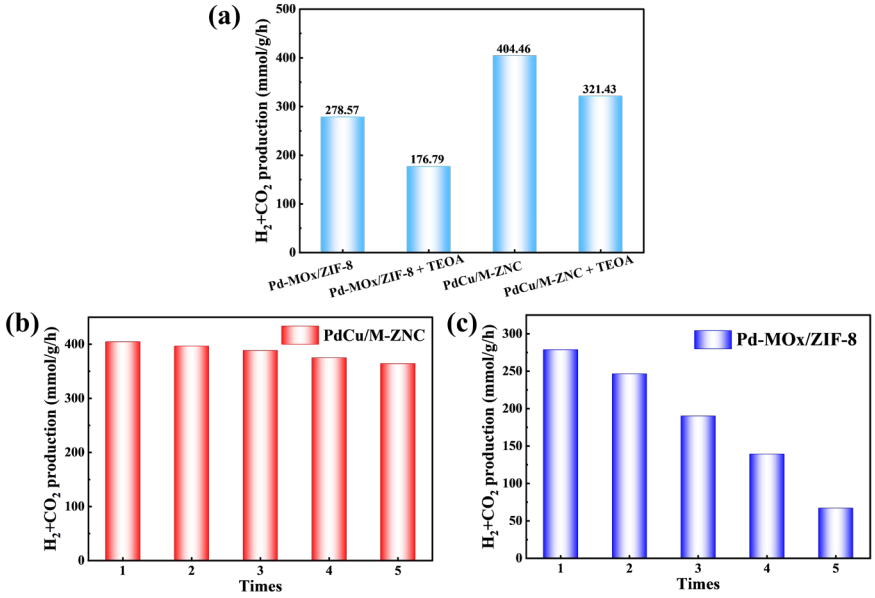

Figure 8. (**a**) Comparison of the gas production rates over the Pd-MO_x/ZIF-8 and PdCu/M-ZNC catalysts in the absence and presence of TEOA. Stability of the (**b**) PdCu/M-ZNC and (**c**) Pd-MO_x/ZIF-8 catalyst for FA dehydrogenation in an FA-SF solution under light irradiation at 75 °C.

To explicitly decouple the photothermal effect from the electronic mechanism, infrared (IR) thermography was performed to evaluate the photothermal conversion behaviors of the catalysts. As illustrated in Figure S6, under continuous illumination, the surface temperatures of both catalysts experienced a moderate rise before reaching a stable plateau. Specifically, the surface temperatures of the Pd-MO_x/ZIF-8 catalyst at 5, 10, and 15 min were 40.70 °C, 55.81 °C and 56.92 °C, respectively. The PdCu/M-ZNC catalyst exhibited slightly higher corresponding temperatures of 42.87 °C, 60.48 °C and 61.22 °C. Notably, the maximum localized photothermal temperature achieved by the PdCu/M-ZNC catalyst was

approximately 61.22 °C, which was substantially lower than the optimal controlled reaction temperature of 75 °C. In the liquid-phase reaction system, the abundant solution served as a highly efficient heat sink, further dissipating any subtle localized heat. Consequently, this moderate photothermal conversion was thermodynamically insufficient to drive the macroscopic increase in the gas generation rate observed at 75 °C. Coupled with the activity suppression observed in the TEOA experiments, these findings demonstrated that the catalytic enhancement upon illumination was predominantly driven by a photo-induced electronic mechanism, rather than a localized thermal acceleration effect.

Furthermore, it was essential to examine the cycling stability of the catalysts. As illustrated in Figure 8b,c, the PdCu/M-ZNC catalyst sustains an exceptionally high level of catalytic activity over five consecutive cycling tests. Post-run characterizations were performed on the spent catalysts. The XRD pattern of the spent PdCu/M-ZNC catalyst (Figure S7a) well preserves the characteristic peaks of the fresh sample, indicating excellent structural robustness. Meanwhile, its specific surface area exhibits only a moderate reduction from 170.1 m^2/g to 114.5 m^2/g (Figure S8a). Moreover, inductively coupled plasma (ICP) analysis (Table S2) revealed that the metal mass fractions in the spent PdCu/M-ZNC remained almost identical to the initial values. Transmission electron microscopy (TEM) observations provided direct visual evidence for morphological evolution. As shown in Figure S9, the average nanoparticle size of the spent PdCu/M-ZNC catalyst only underwent a slight increase from 6.65 ± 1.88 nm to 8.26 ± 1.62 nm compared to the fresh sample. These comprehensive observations corroborate that the marginal attenuation in the gas generation rate was primarily due to this subtle growth and agglomeration of the PdCu nanoparticles under repeated photothermal conditions. In stark contrast, the Pd-MO_x/ZIF-8 catalyst experienced a precipitous deactivation starting from the third cycle. Its specific surface area drastically plummeted from 253.9 m^2/g to 10.5 m^2/g (Figure S8b). ICP analysis (Table S1) further confirmed a substantial loss of the active metal components, with the Pd content dropping significantly from 2.04 wt.% to 0.93 wt.%. TEM images (Figure S10) revealed a catastrophic nanoparticle sintering phenomenon. The highly dispersed metal nanoparticles with an average size of 2.86 ± 1.13 nm in the fresh state severely aggregate into massive solid clusters reaching 45.77 ± 12.66 nm in the spent state. Consequently, this severe performance degradation could be conclusively attributed to the massive active species leaching and severe nanoparticle sintering.

To elucidate the unique synergistic enhancements achieved by our multicomponent design, control catalysts (PdCu/ZNC and Pd/M-ZNC) were prepared and evaluated in photothermal catalytic experiments. As illustrated in Figure 9, under dark conditions, the gas production of PdCu/M-ZNC is significantly higher than that of Pd/M-ZNC. This activity was primarily attributed to the introduction of Cu, which forms a robust alloy with Pd. Extrapolating from the experimental observations, it was postulated that this synergistic alloying effect tailors the electronic structure of the Pd active sites, thereby mitigating the apparent activation energy barrier required for C-H bond cleavage in formic acid [83]. While PdCu/ZNC and PdCu/M-ZNC exhibit comparable performance metrics in the dark, the gas evolution rate and hydrogen selectivity of PdCu/M-ZNC substantially surpass those of PdCu/ZNC under illumination. This photothermal leap is driven by the abundant M-N_x sites, which serve as highly efficient transport pathways for photogenerated electrons. Furthermore, despite its inferior performance under dark conditions, Pd/M-ZNC outperforms PdCu/ZNC upon light irradiation. Based on this experimental phenomenon, it is reasonable to postulate that under photothermal conditions, the kinetic enhancement driven by the M-N_x electron transport network likely outweighs the benefits derived from PdCu alloying.

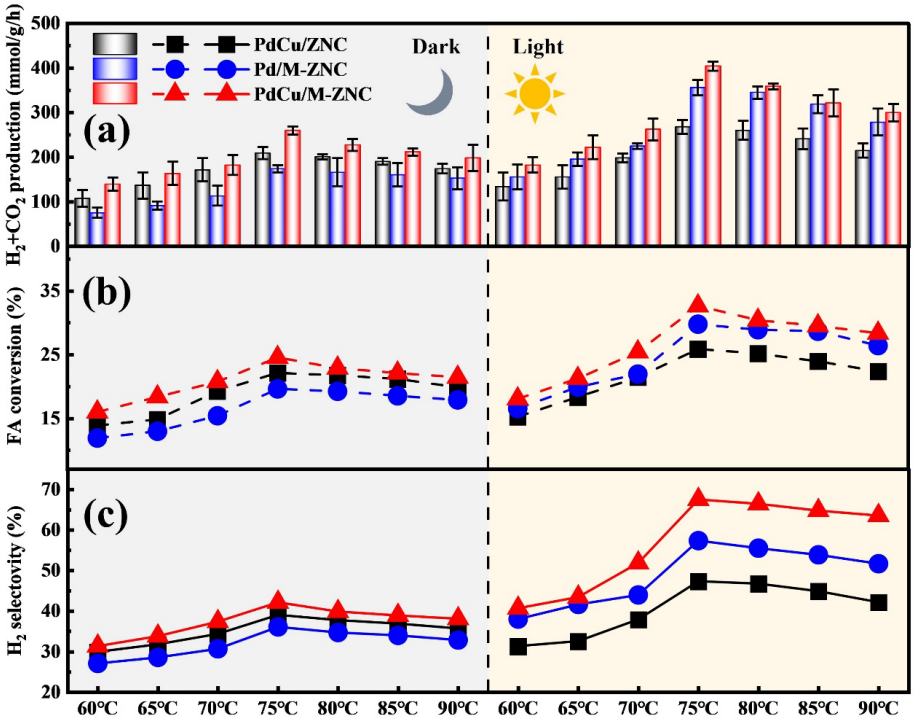

Figure 9. (**a**) H_2 + CO_2 production, (**b**) FA conversion and (**c**) H_2 selectivity of FA dehydrogenation over PdCu/ZNC, Pd/M-ZNC and PdCu/M-ZNC. Reaction conditions: catalyst mass: 0.1 g; reaction solution: 10 mL of an aqueous mixture containing formic acid–sodium formate mixture (n_{FA}:n_{SF} = 1:1, 2 mmol FA); reaction time: 5 min; irradiation: 300 W xenon lamp equipped with an AM 1.5G filter (100 mW cm^{-2}); temperature was controlled via a thermostatic oil bath. The evolved gas volume was quantified using the water displacement method, and the gas composition was analyzed by GC equipped with TCD and FID.

Based on comprehensive experimental results and structural characterizations, a synergistic dual-pathway mechanism is proposed to elucidate the photothermal catalytic performance of PdCu/M-ZNC for formic acid dehydrogenation (Figure 10). The first pathway involves localized thermocatalytic dissociation on the highly dispersed PdCu alloy. Formic acid molecules absorb onto the PdCu surface and undergo consecutive bond cleavages to form critical intermediates, such as H* and HCOO* [84]. The subsequent recombination of adjacent H* species yields H_2. Simultaneously, a parallel photochemical reforming pathway is highly active within the system. The highly graphitized ZNC support enriched with M-N_x sites functions as an efficient light-harvesting and charge-transporting semiconductor matrix. Upon photoexcitation, electron–hole pairs are generated within the M-N_x network. In this specific photochemical process, the reactant formic acid acts as a hole scavenger. It is oxidized by the photogenerated holes (h^+) in the valence band, which effectively suppresses charge recombination while concurrently releasing protons (H^+) and CO_2 [85]. Meanwhile, the photogenerated electrons (e^-) in the conduction band rapidly migrate to the intimately anchored PdCu nanoparticles. Serving as a robust cocatalyst, the PdCu alloy efficiently captures these electrons to drive the rapid reduction of the generated protons into additional H_2. This charge-mediated mechanism, working in concert with localized thermal energy, results in higher activity and selectivity at a lower apparent temperature, embodying the energy-saving advantage of photothermal catalysis.

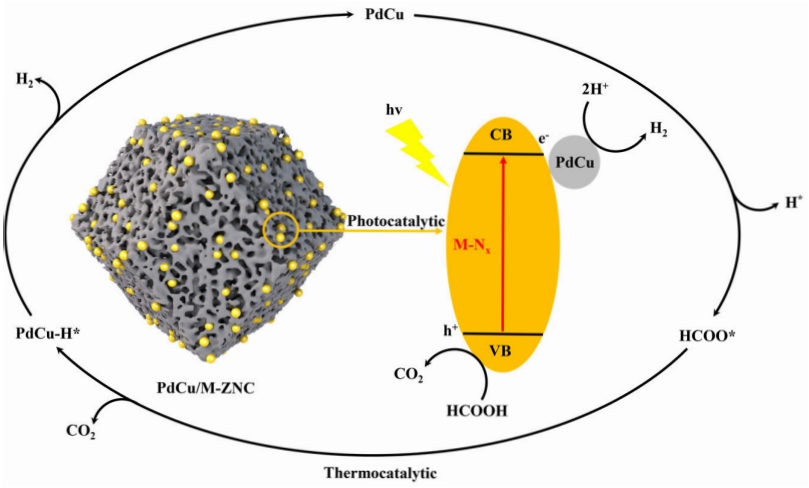

Figure 10. Thermocatalytic and photocatalytic pathways of FA molecules on the surface of the PdCu/M-ZNC catalyst.

3. Experimental Procedure

The synthetic route of the PdCu/M-ZNC catalyst is illustrated in Figure 11. In order to fabricate nitrogen-doped carbon, a KCl-KBr mixture was selected as the molten salt for ZIF-8 pyrolysis instead of pure KCl or KBr. This choice stemmed from the mixture's tunable melting point, high stability across a broad temperature range (717–771 °C) and mild phase transition behavior, which collectively facilitated precise control over the pyrolysis process, mitigated ZIF-8 framework collapse during thermal treatment and thus preserved the material's specific surface area [85].

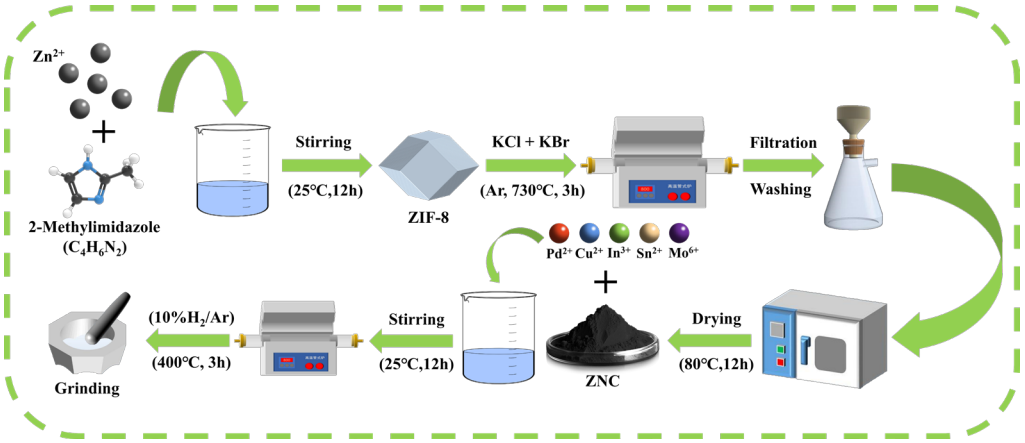

Figure 11. Preparation of PdCu/M-ZNC by molten-salt-assisted pyrolysis method.

3.1. Catalyst Preparation

Zinc acetate dihydrate ($Zn(CH_3COO)_2{\cdot}2H_2O$, 98%), 2-methylimidazole ($C_4H_6N_2$, 98%), palladium chloride ($PdCl_2$ 99.9%-Pd), copper(II) nitrate hydrate ($Cu(NO_3)_2{\cdot}3H_2O$, 98%), indium(III) nitrate hydrate ($In(NO_3)_3{\cdot}5H_2O$ 99%), tin(IV) chloride pentahydrate ($SnCl_4{\cdot}5H_2O$, 99%), ammonium molybdate ($(NH_4)_2MoO_4$, 98%), hydrochloric acid (HCl, 37%), potassium chloride (KCl, 99.5%), and potassium bromide (KBr, 99%) were purchased from Shanghai Macklin Biochemical Co., Ltd. (Shanghai, China). All chemicals were purchased from commercial sources and used without further purification.

3.1.1. Preparation of ZIF-8

An aqueous solution (10 mL) of $Zn(CH_3COO)_2{\cdot}2H_2O$ (600 mg) was added to an aqueous solution of 2-methylimidazole (5.44 mol/L, 13 mL), and the mixture was stirred

at room temperature for 12 h. The mixture was allowed to stand at room temperature for a further 12 h to obtain a white precipitate. The precipitate was then collected by centrifugation, washed three times with deionized water, and dried at 60 °C to obtain ZIF-8.

3.1.2. Preparation of ZNC

The prepared ZIF-8 (1 g) was mixed evenly with KCl-KBr salt (8.75 g of KCl and 26.25 g of KBr, corresponding to a KCl:KBr = 1:3 weight ratio, ZIF-8:KCl-KBr salt = 1:35 [86]), and then the mixture was heated to 730 °C in a tube furnace at a heating rate of 5 °C/min and kept for 3 h under Ar atmosphere. The obtained black product was then washed with 0.2 M HCl aqueous solution and deionized water and denoted as ZNC.

3.1.3. Preparation of PdCu/M-ZNC and Pd-MO_x/ZIF-8 (M = In, Sn and Mo)

To ensure a total loading of 10% for the five metals and a molar ratio of 1:1:1:1:1, $PdCl_2$ (35.5 mg) and $SnCl_4 \cdot 5H_2O$ (70.0 mg) were weighed and dissolved in 5 mL of 0.1 M HCl solution. $Cu(NO_3)_2 \cdot 3H_2O$ (48.4 mg), $In(NO_3)_3 \cdot H_2O$ (60.2 mg), and $(NH_4)_2MoO_4$ (40.1 mg) were weighed and dissolved in 5 mL of deionized water. After mixing the two solutions, 1 g of ZNC carrier was added, and the resulting mixture was stirred at room temperature for 12 h and then dried at 60 °C for 12 h. The dried sample was placed in a 10% H_2/Ar atmosphere and heated to 400 °C at a heating rate of 5 °C/min and held for 3 h to finally obtain the PdCu/M-ZNC composite material. The preparation of PdCu-MO_x/ZIF-8 followed the same method as described above, except that the support was replaced by pure ZIF-8 instead of ZNC, while all other conditions remain unchanged.

3.2. Catalyst Characterizations

The X-ray powder diffraction (XRD, Rigaku Ultima IV, Yokyo, Japan) was implemented to determine the sample phases. A Cu target Kα radiation source (operating at 40 kV and 30 mA, λ = 0.15406 nm) was used. The diffraction angle 2θ was set from 10° to 80° and measured at a scan rate of 5°/min. X-ray photoelectron spectroscopy (XPS, Thermo Scientific Nexsa, Waltham, MA, USA) was employed to analyze the valence distribution of the catalyst. The Brunauer–Emmett–Teller (BET, Micromeritics ASAP 2460, Shanghai, China) method was carried out to obtain the specific surface area and pore structure data. A field emission scanning electron microscope (FESEM, ZEISS Sigma 360, Oberkochen, Germany) was used to study the surface morphology and element distributions of the samples. High-resolution transmission electron microscopy (HRTEM, FEI Talos 200S, Waltham, MA, USA) was carried out to further study the microscopic internal structure of the samples. The functional groups were determined using a Thermo Fisher Scientific Nicolet iS5 (Waltham, MA, USA) Fourier transform infrared spectrometer (FTIR) with a wave number scope of 500–4000 cm^{-1}. The deposited carbon species were identified by a Horiba LabRAM HR Evolution (Palaiseau, France) Raman spectrometer with a laser wavelength of 532 nm at a Raman shift of 50–3500 cm^{-1}. Photoluminescence (PL) spectroscopy was performed using an FLS1000 spectrometer (Edinburgh, UK) with excitation at 468 nm to study charge carrier recombination. Photoelectrochemical measurements were carried out on a CHI760E electrochemical workstation (Shenzhen, China) using a three-electrode system, with Ag/AgCl as a reference electrode, a Pt electrode as the counter electrode, and a 0.5 M Na_2SO_4 solution (pH = 7) as the electrolyte. UV–vis absorption spectra were recorded on a UV-3600 Plus spectrophotometer (Shimadzu, Kyoto, Japan) to evaluate the optical properties.

3.3. Photothermal Reforming Hydrogen Production from Formic Acid

Photothermal catalytic experiments were performed in a three-necked flask under atmospheric pressure, with the reaction temperature regulated by a constant-temperature

oil bath. After adding 0.1 g of catalyst to the flask, the internal gas was evacuated using a vacuum pump followed by nitrogen purging. This evacuation–purging cycle was repeated three times before the flask was sealed with a rubber stopper. A syringe loaded with a formic acid–sodium formate mixture was inserted through the rubber stopper, and the reaction solution was automatically drawn into the flask by the internal negative pressure. A 300 W CEL-HXF-T3 xenon lamp (Beijing, China) served as the light source. The lamp was equipped with an AM 1.5G filter (Beijing, China) to simulate sunlight. The light intensity was calibrated to 100 mW cm^{-2} using a standard silicon photodiode power meter (Newport 1918-R, Shenzhen, China). The distance between the lamp window and the reaction vessel was fixed at 15 cm to ensure uniform irradiation. Control experiments under dark conditions were conducted by wrapping the reaction flask in aluminum foil while maintaining an identical temperature via the oil bath. The total volume of evolved gas was quantified via the water displacement method, while gas composition analysis was conducted using a gas chromatograph equipped with a thermal conductivity detector (TCD) and a flame ionization detector (FID). All catalytic tests were conducted as triplicate parallel experiments.

4. Conclusions

In summary, this work successfully fabricated a polymetallic PdCu/M-ZNC catalyst via a molten-salt-assisted pyrolysis method for efficient photothermal hydrogen production from formic acid. The ZIF-derived nitrogen-doped carbon architecture serves as an effective matrix to stabilize the PdCu alloy nanoparticles while fostering the formation of atomically dispersed M-N_x (where M denotes In, Sn, and Mo) coordination sites. Advanced characterization and comparative experiments reveal a multi-component synergy: the PdCu alloy, M-N_x coordination sites and N-doped carbon framework function cooperatively as a kinetic–electronic–structural triad. Catalytic performance evaluations demonstrated that PdCu/M-ZNC exhibited excellent catalytic activity in formic acid photothermal hydrogen production, significantly outperforming non-pyrolyzed ZIF-8-based catalysts. This enhanced catalytic behavior is attributed to the synergistic interplay among the structural components. The PdCu alloy primarily facilitates the dehydrogenation kinetics, the polymetallic M-N_x sites streamline electron transport, and the nitrogen-doped carbon support ensures stable anchoring alongside efficient mass transfer channels. These three components collectively construct a highly efficient and stable catalytic system. This work provides a rational design strategy for multifunctional photothermal catalysts and demonstrates a sustainable path toward low-temperature, solar-enhanced hydrogen release from liquid organic hydrogen carriers.

Supplementary Materials: The following supporting information can be downloaded at: https://www.mdpi.com/article/10.3390/catal16050385/s1, Figure S1. XRD pattern of PdCu/M-ZNC and Pd/M-ZNC; Figure S2. High-resolution XRD diffraction pattern of Pd-MO_x/ZIF-8; Figure S3. Electrochemical impedance spectra of the PdCu/M-ZNC and Pd-MO_x/ZIF-8 samples; Figure S4. Gas chromatograms of the evolved gases from formic acid over the PdCu/M-ZNC catalyst at various temperatures (60–90 °C) under (a) dark and (b) light conditions. A standard CO gas chromatogram is included at the bottom as a reference; Figure S5. Arrhenius plots for the calculation of apparent activation energies (E_a) based on the pseudo-first-order kinetic rate constants: (a) PdCu/M-ZNC catalyst under dark conditions, (b) PdCu/M-ZNC catalyst under continuous illumination, (c) Pd-MO_x/ZIF-8 catalyst under dark conditions, and (d) Pd-MO_x/ZIF-8 catalyst under continuous illumination; Figure S6. Infrared (IR) thermography images and the corresponding surface temperature evolution of the Pd-MO_x/ZIF-8 and PdCu/M-ZNC catalysts under continuous light irradiation. The temperatures were specifically recorded at irradiation times of 5, 10, and 15 min; Figure S7. XRD patterns of the fresh and spent (a) PdCu/M-ZNC and (b) Pd-MO_x/ZIF-8 catalysts after 5 photothermal cycles at

75 °C; Figure S8. N_2 adsorption-desorption isotherms of the fresh and spent (a) PdCu/M-ZNC and (b) Pd-MO_x/ZIF-8 catalysts after 5 photothermal cycles; Figure S9. Transmission electron microscopy (TEM) images and the corresponding particle size distribution histograms of the (a, b) fresh and (c, d) spent PdCu/M-ZNC catalysts. The spent catalyst was recovered after 5 consecutive photothermal cycles at 75 °C; Figure S10. Transmission electron microscopy (TEM) images and the corresponding particle size distribution histograms of the (a, b) fresh and (c, d) spent Pd-MO_x/ZIF-8 catalysts. The spent catalyst was recovered after 5 consecutive photothermal cycles at 75 °C; Figure S11. Comparison of PdCu/M-ZNC and Pd-MO_x/ZIF-8 catalysts against other previously reported Pd-based systems for photothermal formic acid dehydrogenation; Table S1. Metal mass fractions and molar amounts of fresh catalysts; Table S2. Metal mass fractions and molar amounts of the recovered catalysts after 5 photothermal cycles at 75 °C; Table S3. Turnover frequency (TOF) values of the Pd-MO_x/ZIF-8 catalyst for formic acid dehydrogenation under dark and light conditions at various temperatures; Table S4. Turnover frequency (TOF) values of the PdCu/M-ZNC catalyst for formic acid dehydrogenation under dark and light conditions at various temperatures; Table S5. Formic acid (FA) conversion and H_2 selectivity over the Pd-MO_x/ZIF-8 catalyst at various temperatures under dark and light conditions. Data were presented as mean ± standard deviation; Table S6. Formic acid (FA) conversion and H_2 selectivity over the PdCu/M-ZNC catalyst at various temperatures under dark and light conditions. Data were presented as mean ± standard deviation; Table S7. Formic acid (FA) conversion and H_2 selectivity over the PdCu/ZNC catalyst at various temperatures under dark and light conditions. Data were presented as mean ± standard deviation; Table S8. Formic acid (FA) conversion and H_2 selectivity over the Pd/M-ZNC catalyst at various temperatures under dark and light conditions. Data were presented as mean ± standard deviation; Table S9. Performance comparison of Pd-based catalysts for formic acid dehydrogenation.

Author Contributions: S.L.: Preparation experiments; Writing original draft. S.S.: Investigation. C.K.: Investigation. Z.G.: Responsible for resources. M.L.: Writing review; Editing. C.W.: Responsible for the methodology. All authors have read and agreed to the published version of the manuscript.

Funding: This work was supported by the funding of Natural Science Foundation of China (No.22578070, No.22378073) and Guangzhou Basic and Applied Basic Research Foundation (SL2024A04J00939). We also thank all the colleagues and students who have contributed to this work in this area.

Data Availability Statement: The data used in this study are available in this paper.

Acknowledgments: The authors would like to express their sincere gratitude to Yili Xiao for his expert assistance with the XRD data analysis.

Conflicts of Interest: The authors declare no conflict of interest.

References

1. Mehtab, A.; Ali, S.A.; Sadiq, I.; Shaheen, S.; Khan, H.; Fazil, M.; Pandit, N.A.; Naaz, F.; Ahmad, T. Hydrogen Energy as Sustainable Energy Resource for Carbon-Neutrality Realization. *ACS Sustain. Resour. Manag.* **2024**, *1*, 604. [CrossRef]
2. Bhuiyan, M.M.H.; Siddique, Z. Hydrogen as an alternative fuel: A comprehensive review of challenges and opportunities in production, storage, and transportation. *Int. J. Hydrogen Energy* **2025**, *102*, 1026–1044. [CrossRef]
3. Kazemi, A.; Manteghi, F.; Tehrani, Z. Metal electrocatalysts for hydrogen production in water splitting. *ACS Omega* **2024**, *9*, 7310–7335. [CrossRef]
4. Chaturvedi, A.; Shah, M.; Sogani, M.; Subbaramaiah, V. Highly competent hydrogen evolution cathode catalyst in microbial electrolysis Cell: Recent advances and Emerging challenges. *Sustain. Energy Technol. Assess.* **2026**, *88*, 104945. [CrossRef]
5. Wesley, G.; Swetlech, E.; Velasco, C.; Williams, A.; Larsen, K.; Antony Jose, S.; Menezes, P.L. Catalytic Materials for Hydrogen Generation: Design, Properties, and Applications in Sustainable Energy Systems. *Processes* **2026**, *14*, 957. [CrossRef]
6. Impemba, S.; Provinciali, G.; Filippi, J.; Caporali, S.; Muzzi, B.; Casini, A.; Caporali, M. Tightly Interfaced Cu_2O with In_2O_3 to Promote Hydrogen Evolution in Presence of Biomass-Derived Alcohols. *ChemNanoMat* **2024**, *10*, e202400459. [CrossRef]
7. Kumar, R.; Swain, G.; Dutta, S. Recent Advances in H_2 Production by Photocatalytic Water Splitting. In *Towards Sustainable and Green Hydrogen Production by Photocatalysis: Scalability Opportunities and Challenges (Volume 1)*; ACS Publications: Washington, DC, USA, 2024; pp. 47–68.

8. Zhou, J.; Tian, Y.; Gu, H.; Jiang, B. Photocatalytic hydrogen evolution: Recent advances in materials, modifications, and photothermal synergy. *Int. J. Hydrogen Energy* **2025**, *115*, 113–130. [CrossRef]
9. Impemba, S.; Provinciali, G.; Filippi, J.; Salvatici, C.; Berretti, E.; Caporali, S.; Banchelli, M.; Caporali, M. Engineering the heterojunction between TiO_2 and In_2O_3 for improving the solar-driven hydrogen production. *Int. J. Hydrogen Energy* **2024**, *63*, 896–904. [CrossRef]
10. Deka, D.J.; Boruah, B.; Lee, G.; Rappé, K.G. Recent advances in ammonia decomposition technologies for hydrogen production. *Energy Fuels* **2025**, *39*, 10802–10852. [CrossRef]
11. Ghoreishian, S.M.; Norouzi, M.; Lauterbach, J. Recent progress in the decomposition of ammonia as a potential hydrogen-carrier using green technologies. *Chem. Commun.* **2025**, *61*, 8969–8983. [CrossRef]
12. Zhang, H.; Liu, Y.; Liu, S.; Guan, S.; Shen, R.; Wen, H.; Cao, X.; Liu, B.; Jiang, J.; Li, B. Progress and Perspective on Heterogeneous Catalysis of Liquid Formic Acid Dehydrogenation: Coordination Structure Design, Activity Improvement, and Mechanism Insights. *Adv. Mater.* **2025**, *37*, e09068. [CrossRef] [PubMed]
13. Edor, J.M.; Joseph, M.C.; Jordaan, J.H.L.; Vosloo, H.C.M.; Swarts, A.J. Formic Acid Dehydrogenation Catalysis Using Novel Pyridyl-Formamidine Half-Sandwich Ruthenium(II) Complexes. *Appl. Organomet. Chem.* **2025**, *39*, e70016. [CrossRef]
14. Li, X.; Guan, X.; Zhu, L.; Li, H.; Yin, X.; Sun, S.; Xu, H.; Fan, Y.; Li, P.; Hu, L.; et al. Electron transfer in catalysis: From fundamentals to strategies. *Chem. Soc. Rev.* **2025**, *54*, 11423. [CrossRef]
15. Meng, X.; Liu, L.; Ouyang, S.; Xu, H.; Wang, D.; Zhao, N.; Ye, J. Nanometals for Solar-to-Chemical Energy Conversion: From Semiconductor-Based Photocatalysis to Plasmon-Mediated Photocatalysis and Photo-Thermocatalysis. *Adv. Mater.* **2016**, *28*, 6781. [CrossRef] [PubMed]
16. Lin, L.; Wang, K.; Yang, K.; Chen, X.; Fu, X.; Dai, W. The visible-light-assisted thermocatalytic methanation of CO_2 over $Ru/TiO_{(2-x)}N_x$. *Appl. Catal. B Environ.* **2017**, *204*, 440. [CrossRef]
17. Fan, P.; He, Y.; Pan, J.; Sun, N.; Zhang, Q.; Gu, C.; Chen, K.; Yin, W.; Wang, L. Recent advances in photothermal effects for hydrogen evolution. *Chin. Chem. Lett.* **2024**, *35*, 108513. [CrossRef]
18. Ma, R.; Sun, J.; Li, D.H.; Wei, J.J. Review of synergistic photo-thermo-catalysis: Mechanisms, materials and applications. *Int. J. Hydrogen Energy* **2020**, *45*, 30288. [CrossRef]
19. Han, L.; Zhang, L.; Wu, H.; Zu, H.; Cui, P.; Guo, J.; Guo, R.; Ye, J.; Zhu, J.; Zheng, X.; et al. Anchoring Pt Single Atoms on Te Nanowires for Plasmon-Enhanced Dehydrogenation of Formic Acid at Room Temperature. *Adv. Sci.* **2019**, *6*, 1900006. [CrossRef]
20. Zhang, D.; Zhao, F.; Lv, C.; Xu, M.; Gao, L.; Ning, S.; Hao, Y.; Li, Y.; Ye, J. Molten salt etching route driven universal construction of MXene/nickel hybrids for photothermal catalytic formic acid dehydrogenation. *Appl. Surf. Sci.* **2025**, *708*, 163674. [CrossRef]
21. Mancuso, A.; Diglio, M.; Impemba, S.; Venditto, V.; Vaiano, V.; Buonerba, A.; Sacco, O. Dual-Function Bare Copper Oxide (Photo) Catalysts for Selective Phenol Production via Benzene Hydroxylation and Low-Temperature Hydrogen Generation from Formic Acid. *Catalysts* **2025**, *15*, 866. [CrossRef]
22. Pechenkin, A.; Badmaev, S.; Belyaev, V.; Sobyanin, V. Production of hydrogen-rich gas by formic acid decomposition over $CuO\text{-}CeO_2/\gamma\text{-}Al_2O_3$ catalyst. *Energies* **2019**, *12*, 3577. [CrossRef]
23. Diglio, M.; Contento, I.; Impemba, S.; Berretti, E.; Della Sala, P.; Oliva, G.; Naddeo, V.; Caporali, S. Hydrogen production from formic acid decomposition promoted by gold nanoparticles supported on a porous polymer matrix. *Energy Fuels* **2025**, *39*, 14320–14329. [CrossRef] [PubMed]
24. Yi, N.; Saltsburg, H.; Flytzani-Stephanopoulos, M. Hydrogen production by dehydrogenation of formic acid on atomically dispersed gold on ceria. *ChemSusChem* **2013**, *6*, 816–819. [CrossRef]
25. Jeon, H.; Chung, Y.M. Hydrogen production from formic acid dehydrogenation over Pd/C catalysts: Effect of metal and support properties on the catalytic performance. *Appl. Catal. B Environ.* **2017**, *210*, 212. [CrossRef]
26. Mori, K.; Tanaka, H.; Dojo, M.; Yoshizawa, K.; Yamashita, H. Synergic Catalysis of PdCu Alloy Nanoparticles within a Macroreticular Basic Resin for Hydrogen Production from Formic Acid. *Chemistry* **2015**, *21*, 12085. [CrossRef]
27. Zhu, Y.; Ma, H.; Qian, W.; Zhang, H.; Zhang, H.; Ying, W. Co- and Ni-promoted indium oxide for CO_2 hydrogenation to methanol. *Catal. Sci. Technol.* **2024**, *14*, 3771. [CrossRef]
28. Zhang, W.; Mao, Q.; Ding, J.; Liu, Q.; Wang, S.; Wang, J.; Li, X.; Yang, H.; Liu, B. S-doped Ag-Sn Alloy Hollow Microbox for High-Performance CO_2 Electroreduction to Formate. *Angew. Chem. Int. Ed.* **2025**, *64*, e202510743.
29. Hu, X.; Ding, C.; Chen, C.; Yang, Y.; Zhang, X.; Li, X.; Chen, B.; Wang, N. Mo-tailored CoFe alloy catalysts: Overcoming over-carburization via suppressing CO dissociation and tuning CHx coupling for selective higher alcohol synthesis. *Appl. Catal. B Environ. Energy* **2025**, *377*, 125515. [CrossRef]
30. Xu, M.; Peng, M.; Tang, H.; Zhou, W.; Qiao, B.; Ma, D. Renaissance of Strong Metal–Support Interactions. *J. Am. Chem. Soc.* **2024**, *146*, 2290. [CrossRef] [PubMed]
31. Dong, Q.; Li, X.; Duan, Y.; Tian, Q.; Liang, X.; Zhu, Y.; Tian, L.; Wang, J.; Sial, A.; Cui, Y.; et al. Recent advances in core-shell organic framework-based photocatalysts for energy conversion and environmental remediation. *J. Energy Chem.* **2024**, *95*, 168–199. [CrossRef]

32. Huang, Y.; Chen, Y.; Xu, M.; Ly, A.; Gili, A.; Murphy, E.; Asset, T.; Liu, Y.; De Andrade, V.; Segre, C.U. Catalysts by pyrolysis: Transforming metal-organic frameworks (MOFs) precursors into metal-nitrogen-carbon (M-N-C) materials. *Mater. Today* **2023**, *69*, 66. [CrossRef]
33. Wan, K.; Tan, A.; Yu, Z.; Liang, Z.; Piao, J.; Tsiakaras, P. 2D nitrogen-doped hierarchically porous carbon: Key role of low dimensional structure in favoring electrocatalysis and mass transfer for oxygen reduction reaction. *Appl. Catal. B Environ.* **2017**, *209*, 447. [CrossRef]
34. Sun, J.F.; Xu, Q.Q.; Qi, J.L.; Zhou, D.; Zhu, H.Y.; Yin, J.Z. Isolated Single Atoms Anchored on N-Doped Carbon Materials as a Highly Efficient Catalyst for Electrochemical and Organic Reactions. *ACS Sustain. Chem. Eng.* **2020**, *8*, 14630. [CrossRef]
35. Avci, C.; Imaz, I.; Carné-Sánchez, A.; Pariente, J.A.; Tasios, N.; Pérez-Carvajal, J.; Alonso, M.I. Self-assembly of polyhedral metal–organic framework particles into three-dimensional ordered superstructures. *Nat. Chem.* **2018**, *10*, 78. [CrossRef] [PubMed]
36. Pang, S.H.; Han, C.; Sholl, D.S.; Jones, C.W.; Lively, R.P. Facet-specific stability of ZIF-8 in the presence of acid gases dissolved in aqueous solutions. *Chem. Mater.* **2016**, *28*, 6960. [CrossRef]
37. Bhattacharyya, S.; Han, R.; Kim, W.G.; Chiang, Y.; Jayachandrababu, K.C.; Hungerford, J.T.; Dutzer, M.; Ma, C.; Walton, K.; Sholl, D.; et al. Acid gas stability of zeolitic imidazolate frameworks: Generalized kinetic and thermodynamic characteristics. *Chem. Mater.* **2018**, *30*, 4089. [CrossRef]
38. Ta, D.N.; Nguyen, H.K.D.; Trinh, B.X.; Le, Q.T.; Ta, H.N.; Nguyen, H.T. Preparation of nano-ZIF-8 in methanol with high yield. *Can. J. Chem. Eng.* **2018**, *96*, 1518. [CrossRef]
39. Sun, Y.; Wang, Y.; Li, C.; Zhang, Q.; Wang, L.; Lv, Q.; Feng, S. Heteroatom-Doping Modulates Metal-Support Interactions in Carbon-Supported Cobalt Catalysts to Accelerate Polysulfide Redox for Lithium–Sulfur Batteries. *Adv. Funct. Mater.* **2025**, *35*, 2421780. [CrossRef]
40. Ashraf, S.; Liu, Y.; Liu, S.; Mehdi, S.; Zhang, H.; Shen, R.; Guo, X.; Wu, X.; Jiang, J.; Wang, Y.; et al. Synergistic Electronic Interaction in PdCu Alloy/TiO2-NSs for Ambient Efficient Dehydrogenation of Formic Acid. *Small* **2025**, *21*, 2407922. [CrossRef]
41. Lin, Y.; Liu, Y.; Li, Y.; Cao, Y.; Huang, J.; Wang, H.; Yu, H.; Liang, H.; Peng, F. Dual functional CuO_{1-x} clusters for enhanced photocatalytic activity and stability of a Pt cocatalyst in an overall water-splitting reaction. *ACS Sustain. Chem. Eng.* **2018**, *6*, 17340. [CrossRef]
42. Gallagher, J.R.; Li, T.; Zhao, H.; Liu, J.; Lei, Y.; Zhang, X.; Ren, Y.; Elam, J.W.; Meyer, R.J.; Winans, R.E.; et al. In situ diffraction of highly dispersed supported platinum nanoparticles. *Catal. Sci. Technol.* **2014**, *4*, 3053. [CrossRef]
43. Li, Y.; Zhou, K.; He, M.; Yao, J. Synthesis of ZIF-8 and ZIF-67 using mixed-base and their dye adsorption. *Microporous Mesoporous Mater.* **2016**, *234*, 287. [CrossRef]
44. Tran, B.L.; Chin, H.Y.; Chang, B.K.; Chiang, A.S. Dye adsorption in ZIF-8: The importance of external surface area. *Microporous Mesoporous Mater.* **2019**, *277*, 149. [CrossRef]
45. Ganesan, A.; Leisen, J.; Thyagarajan, R.; Sholl, D.S.; Nair, S. Hierarchical ZIF-8 materials via acid gas-induced defect sites: Synthesis, characterization, and functional properties. *ACS Appl. Mater. Interfaces* **2023**, *15*, 40623. [CrossRef]
46. Tanaka, S.; Fujita, K.; Miyake, Y.; Miyamoto, M.; Hasegawa, Y.; Makino, T.; Perre, S.; Remi, J.; Assche, T.; Baron, G.; et al. Adsorption and Diffusion Phenomena in Crystal Size Engineered ZIF-8 MOF. *J. Phys. Chem. C* **2015**, *119*, 28430. [CrossRef]
47. Kumari, G.; Jayaramulu, K.; Maji, T.K.; Narayana, C. Temperature Induced Structural Transformations and Gas Adsorption in the Zeolitic Imidazolate Framework ZIF-8: A Raman Study. *J. Phys. Chem. A* **2013**, *117*, 11006. [CrossRef] [PubMed]
48. Farid, M.A.A.; Zheng, A.L.; Tsubota, T.; Andou, Y. Catalytic graphitization of biomass-derived ethanosolv lignin using Fe, Co, Ni, and Zn: Microstructural and chemical characterization. *J. Anal. Appl. Pyrolysis* **2023**, *173*, 106064. [CrossRef]
49. Guan, L.; Hu, H.; Li, L.; Pan, Y.; Zhu, Y.; Li, Q.; Guo, H.; Wang, K.; Huang, Y.; Zhang, M.; et al. Intrinsic Defect-Rich Hierarchically Porous Carbon Architectures Enabling Enhanced Capture and Catalytic Conversion of Polysulfides. *ACS Nano* **2020**, *14*, 6222. [CrossRef]
50. Zhu, Z.S.; Zhong, S.; Cheng, C.; Zhou, H.; Sun, H.; Duan, X.; Wang, S. Microenvironment Engineering of Heterogeneous Catalysts for Liquid-Phase Environmental Catalysis. *Chem. Rev.* **2024**, *124*, 11348. [CrossRef]
51. Chen, J.; Gu, A.; Miensah, E.D.; Liu, Y.; Wang, P.; Mao, P.; Gong, C.; Jiao, Y.; Chen, K.; Yang, Y. Cu-Zn bimetal ZIFs derived nanowhisker zero-valent copper decorated ZnO nanocomposites induced oxygen activation for high-efficiency iodide elimination. *J. Hazard. Mater.* **2021**, *416*, 126097. [CrossRef]
52. Ahmad, M.; Patel, R.; Lee, D.T.; Corkery, P.; Kraetz, A.; Prerna, N.; Tenney, S.A.; Nykypanchuk, D.; Tong, X.; Siepmann, J.; et al. ZIF-8 Vibrational Spectra: Peak Assignments and Defect Signals. *ACS Appl. Mater. Interfaces* **2024**, *16*, 27887. [CrossRef]
53. Chen, J.; Gao, C.; Chen, J.; Liu, F.; Liu, Z. Cu^0-Functionalized, ZIF-8-Derived, Nitrogen-Doped Carbon Composites for Efficient Iodine Elimination in Solution. *Nanomaterials* **2025**, *15*, 105. [CrossRef]
54. Alam, N.; Noor, T.; Habib, U.; Iqbal, N.; Gao, J. Intrinsic Zn sites in ZIF-8 derived N-doped carbon as active sites for hydrogen evolution reaction. *Int. J. Hydrogen Energy* **2025**, *189*, 152171. [CrossRef]

55. Xiang, X.; Zhang, X.; Yan, B.; Wang, K.; Wang, Y.; Lyu, D.; Xi, S.; Tian, Z.Q.; Shen, P.K. Atomic iron coordinated by nitrogen doped carbon nanoparticles synthesized via a synchronous complexation-polymerization strategy as efficient oxygen reduction reaction electrocatalysts for zinc-air battery and fuel cell application. *Chem. Eng. J.* **2022**, *440*, 135721. [CrossRef]
56. Banerjee, A.C.; Olowookere, I.T.; Cushing, D.; Salamanca, S.T.; Knox, E.; Jackson, T.; Bamonte, S.; Aderibigbe, A.; Silva, D.; Suib, S.L. Hydroperoxyl-bicarbonate mechanism for low-temperature CO oxidation by PdO/CeOx/γ-Al_2O_3 mesoporous nanocatalysts. *RSC Adv.* **2025**, *15*, 36642. [CrossRef]
57. Yang, N.; Zhang, Z.; Chen, B.; Huang, Y.; Chen, J.; Lai, Z.; Chen, Y.; Sindoro, M.; Wang, A.L.; Cheng, H.; et al. Synthesis of Ultrathin PdCu Alloy Nanosheets Used as a Highly Efficient Electrocatalyst for Formic Acid Oxidation. *Adv. Mater.* **2017**, *29*, 1700769. [CrossRef]
58. Jiang, Y.; Jiang, H.; Zhu, Y.; Ye, L.; Zhu, H.; Liu, Z.; Xiao, Y.; Kong, Y.; Ouyang, M.; Wei, Q.; et al. Electronic Structure Engineering of Pd–Cu Alloy Catalysts for Enhanced Methanol Electrooxidation. *Inorg. Chem.* **2025**, *64*, 24787. [CrossRef] [PubMed]
59. Bhuvanendran, N.; Srinivasadesikan, V.; Dharmaraj, V.; Jung, W.G.; Moon, W.J.; Park, C.W.; Lin, M.C.; Lee, S. Ultra-thin dealloyed PdCu bimetallene with lattice strain transformation for efficient bifunctional electrocatalysis. *Int. J. Hydrogen Energy* **2025**, *98*, 514. [CrossRef]
60. Tan, Q.; Zhu, H.; Guo, S.; Chen, Y.; Jiang, T.; Shu, C.; Chong, S.; Hultman, B.; Liu, Y.; Wu, G. Quasi-zero-dimensional cobalt-doped CeO_2 dots on Pd catalysts for alcohol electro-oxidation with enhanced poisoning-tolerance. *Nanoscale* **2017**, *9*, 12565–12572. [CrossRef] [PubMed]
61. Wang, J.; Zhang, G.; Liu, H.; Li, Z.; Wang, L.; Tressel, J.; Chen, S. High-performance electrocatalytic reduction of CO_2 to CO by ultrathin PdCu alloy nanosheets. *Sep. Purif. Technol.* **2023**, *320*, 124186. [CrossRef]
62. Wang, S.; Feng, K.; Zhang, D.; Yang, D.; Xiao, M.; Zhang, C.; He, L.; Yan, B.; Ozin, G.; Sun, W. Stable Cu catalysts supported by two-dimensional SiO_2 with strong metal–support interaction. *Adv. Sci.* **2022**, *9*, 2104972. [CrossRef]
63. Liu, X.; Xie, Y.; Hao, M.; Chen, Z.; Yang, H.; Waterhouse, G.I.; Ma, S.; Wang, X. Highly Efficient Electrocatalytic Uranium Extraction from Seawater over an Amidoxime-Functionalized In–N–C Catalyst. *Adv. Sci.* **2022**, *9*, 2201735. [CrossRef]
64. Guo, W.; Tan, X.; Bi, J.; Xu, L.; Yang, D.; Chen, C.; Zhu, Q.; Ma, J.; Tayal, A.; Ma, J.; et al. Atomic indium catalysts for switching CO2 electroreduction products from formate to CO. *J. Am. Chem. Soc.* **2021**, *143*, 6877. [CrossRef] [PubMed]
65. Li, S.; Lu, X.; Zhao, S.; Ceccato, M.; Hu, X.M.; Roldan, A.; Liu, M.; Daasbjerg, K. p-Block indium single-atom catalyst with low-coordinated In–N motif for enhanced electrochemical CO_2 reduction. *ACS Catal.* **2022**, *12*, 7386. [CrossRef]
66. Li, Q.; Fu, J.; Zhu, W.; Chen, Z.; Shen, B.; Wu, L.; Xi, Z.; Wang, T.; Lu, G.; Zhu, J. Tuning Sn-Catalysis for Electrochemical Reduction of CO_2 to CO via the Core/Shell Cu/SnO_2 Structure. *J. Am. Chem. Soc.* **2017**, *139*, 4290. [CrossRef]
67. Hu, P.; Yang, F.F.; Yang, F.; Zhu, F.; Luo, J.; Chen, X.; Li, W.; Bian, J.; Gao, L.; Wang, K.; et al. Bimetallic organic framework derived Co-Mo_xN/Mo_2C catalyst for HER/OER bifunctional electrocatalytic reaction. *J. Colloid Interface Sci.* **2025**, *680*, 427. [CrossRef]
68. Wang, L.; Zhou, L.; Zheng, X.; Wu, J.; Wang, C.; Yuan, Y.; Jia, X.; Zheng, J. Atomic-Scale Structural Engineering of Carbon-Supported Asymmetric Active Sites: Synergistic Enhancement in Electrocatalysis. *Adv. Funct. Mater.* **2025**, *36*, e21339. [CrossRef]
69. Sachs, M.; Cha, H.; Kosco, J.; Aitchison, C.M.; Francàs, L.; Corby, S.; Chiang, C.L.; Wilson, A.A.; Godin, R.; Williams, A.; et al. Tracking Charge Transfer to Residual Metal Clusters in Conjugated Polymers for Photocatalytic Hydrogen Evolution. *J. Am. Chem. Soc.* **2020**, *142*, 14574. [CrossRef]
70. Chen, J.; Zhang, Y.; Zhang, Z.; Hou, D.; Bai, F.; Han, Y.; Zhang, C.; Zhang, Y.; Hu, J. Metal–support interactions for heterogeneous catalysis: Mechanisms, characterization techniques and applications. *J. Mater. Chem. A* **2023**, *11*, 8540. [CrossRef]
71. Yang, Q.; Cui, P.; Liu, C.; Fang, G.; Dang, F.; Wang, P.; Wang, S.; Wang, Y. Core–shell CoN@Co ultra-stable nanoparticles on biochar for contamination remediation in water and soil. *Carbon Res.* **2024**, *3*, 32. [CrossRef]
72. Zhou, P.; Lv, F.; Li, N.; Zhang, Y.; Mu, Z.; Tang, Y.; Lai, J.; Chao, Y.; Luo, M.; Lin, F.; et al. Strengthening reactive metal-support interaction to stabilize high-density Pt single atoms on electron-deficient g-C_3N_4 for boosting photocatalytic H_2 production. *Nano Energy* **2019**, *56*, 127–137. [CrossRef]
73. Tian, F.; Li, W.; Chen, R.; Yang, J.; Li, Q.; Ran, W.; Li, N.; Du, D.; Yan, T. Electron Transport Chains Promote Selective Photocatalytic Conversion of CO2 to Methanol. *Inorg. Chem.* **2024**, *64*, 460. [CrossRef] [PubMed]
74. Wang, H.; Wang, Z.; Zhang, Z.; Fan, Y.; Fu, X.; Dai, W. Enhanced photocatalytic hydrogen production from formic acid with reversible electron transfers in PdO/TiO_2. *Fuel* **2024**, *362*, 130865. [CrossRef]
75. Zhang, Z.; Wang, M.; Zhou, H.; Wang, F. Surface Sulfate Ion on CdS Catalyst Enhances Syngas Generation from Biopolyols. *J. Am. Chem. Soc.* **2021**, *143*, 6533. [CrossRef]
76. Xu, R.; Lu, W.; Toan, S.; Zhou, Z.; Russell, C.K.; Sun, Z.; Sun, Z. Thermocatalytic formic acid dehydrogenation: Recent advances and emerging trends. *J. Mater. Chem. A* **2021**, *9*, 24241. [CrossRef]
77. Wang, Q.; Lin, S.; Luo, H.; Yu, W.; Liu, W.; Chen, F.; Cheng, D. Enhanced photocatalytic dehydrogenation of formic acid over ultrafine electron-deficient Pd nanoparticles immobilized on amine-functionalized mesoporous titanium dioxide. *Int. J. Hydrogen Energy* **2024**, *77*, 1307–1316. [CrossRef]

78. Wen, M.; Mori, K.; Kuwahara, Y.; Yamashita, H. Plasmonic Au@Pd nanoparticles supported on a basic metal–organic framework: Synergic boosting of H_2 production from formic acid. *ACS Energy Lett.* **2017**, *2*, 1. [CrossRef]
79. Jiang, Y.; Fan, X.; Chen, M.; Xiao, X.; Zhang, Y.; Wang, C.; Chen, L. AuPd nanoparticles anchored on nitrogen-decorated carbon nanosheets with highly efficient and selective catalysis for the dehydrogenation of formic acid. *J. Phys. Chem. C* **2018**, *122*, 4792. [CrossRef]
80. Martin, C.; Quintanilla, A.; Vega, G.; Casas, J.A. Formic acid-to-hydrogen on Pd/AC catalysts: Kinetic study with catalytic deactivation. *Appl. Catal. B Environ.* **2022**, *317*, 121802. [CrossRef]
81. Cao, X.; Du, W.; Zhu, S.; Lin, Y.; Gui, Y.; Liu, L. Photoelectron injection sustains persistent electron-rich Pd for beyond-classical thermocatalytic formic acid dehydrogenation. *Chem. Eng. J.* **2025**, *524*, 169220. [CrossRef]
82. Hamoud, H.I.; Wolski, L.; Abdelli, H.; Chtourou, R.; Lebedev, O.; Martin, C.; Fan, D.; Maurin, G.; Maignan, A.; Ei-Roz, M. Earth-abundant-based photocatalysts for efficient and selective h2 production through reforming of formic acid under visible light. *ACS Catal.* **2023**, *13*, 16266. [CrossRef]
83. Wang, H.; Wang, Z.; Liu, X.; Gao, N.; Song, X.; Zhao, Z. AuPd nanocatalysts supported on citric acid-modified boron nitride to boost hydrogen generation from formic acid dehydrogenation. *ACS Appl. Nano Mater.* **2023**, *6*, 3285. [CrossRef]
84. Liu, X.; Sun, Z.; Chen, Y.L.; Liu, K.; Usman, M.; Gloag, L.; Yin, Z. Pt single atoms/g-C_3N_4 photocatalysts enabling simultaneous H_2 production and CO_2 absorption through formic acid photoreforming. *J. Mater. Chem. A* **2026**. [CrossRef]
85. Zhao, X.; Kong, X.; Wang, F.; Fang, R.; Li, Y. Metal Sub-nanoclusters Confined within Hierarchical Porous Carbons with High Oxidation Activity. *Angew. Chem. Int. Ed.* **2021**, *60*, 10842. [CrossRef]
86. Zhao, X.; Wang, F.; Kong, X.P.; Fang, R.; Li, Y. Dual-Metal Hetero-Single-Atoms with Different Coordination for Efficient Synergistic Catalysis. *J. Am. Chem. Soc.* **2021**, *143*, 16068. [CrossRef]